

General Disclaimer

One or more of the Following Statements may affect this Document

- This document has been reproduced from the best copy furnished by the organizational source. It is being released in the interest of making available as much information as possible.
- This document may contain data, which exceeds the sheet parameters. It was furnished in this condition by the organizational source and is the best copy available.
- This document may contain tone-on-tone or color graphs, charts and/or pictures, which have been reproduced in black and white.
- This document is paginated as submitted by the original source.
- Portions of this document are not fully legible due to the historical nature of some of the material. However, it is the best reproduction available from the original submission.

Tmx 71308
**A COMPUTER SOFTWARE SYSTEM
FOR THE GENERATION OF GLOBAL
OCEAN TIDES INCLUDING
SELF-GRAVITATION AND
CRUSTAL LOADING EFFECTS**

(NASA-TM-X-71308) A COMPUTER SOFTWARE
SYSTEM FOR THE GENERATION OF GLOBAL OCEAN
TIDES INCLUDING SELF-GRAVITATION AND CRUSTAL
LOADING EFFECTS (NASA) 63 p HC A04/MF A01

N77-23709

CSCL 08C G3/48

Unclas
28947

RONALD H. ESTES

APRIL 1977



**GODDARD SPACE FLIGHT CENTER
GREENBELT, MARYLAND**

A COMPUTER SOFTWARE SYSTEM
FOR THE GENERATION OF GLOBAL
OCEAN TIDES INCLUDING SELF-
GRAVITATION AND CRUSTAL LOADING
EFFECTS

R. H. Estes

BUSINESS AND TECHNOLOGICAL SYSTEMS, INC.

March 1977

GODDARD SPACE FLIGHT CENTER
GREENBELT, MARYLAND

A COMPUTER SOFTWARE SYSTEM FOR THE GENERATION OF GLOBAL OCEAN TIDES INCLUDING SELF- GRAVITATION AND CRUSTAL LOADING EFFECTS

R. H. Estes

BUSINESS AND TECHNOLOGICAL SYSTEMS, INC.

ABSTRACT

A computer software system is described which computes global numerical solutions of the integro-differential Laplace Tidal Equations, including dissipation terms and ocean loading and self-gravitation effects, for arbitrary diurnal and semidiurnal tidal constituents. The integration algorithm features a successive approximation scheme for the integro-differential system, with time stepping forward differences in the time variable and central differences in spatial variables. Solutions for M_2 , S_2 , N_2 , K_2 , K_1 , Q_1 , P_1 tidal constituents neglecting the effects of ocean loading and self-gravitation and a converged M_2 solution including ocean loading and self-gravitation effects are presented in the form of cotidal and corange maps.

TABLE OF CONTENTS

	<u>Page</u>
1.0 INTRODUCTION	1
2.0 LAPLACE TIDAL EQUATIONS	3
3.0 TIDAL POTENTIAL EXPANSION	10
4.0 COMPUTATIONAL TECHNIQUES	14
4.1 Hansen Grid	14
4.2 Finite-Difference Formulation	14
4.3 Stability	18
4.4 Integration Algorithm and Solution Representation .	19
4.5 Evaluation of Green's Functions for Ocean Loading .	21
4.6 Tidal Solutions Neglecting Loading and Self- Gravitation Effects	24
4.7 M_2 Tide Including Ocean Loading and Self- Gravitation	38
4.8 Total Tide Comparison with Observations	44
5.0 COMPUTER SOFTWARE SYSTEM	49
5.1 Program Input	49
5.2 Program Output	56
6.0 ACKNOWLEDGEMENT	57
7.0 REFERENCES	58

1.0 INTRODUCTION

Future NASA geodynamic and oceanographic programs depend on extremely accurate knowledge of the geoid. Much of this knowledge will come from highly accurate altimeter measurements from future satellite missions (i.e., SEASAT). The full use of this data necessitates realistic models of the global ocean tides for both the reduction of altimeter data to mean sea level and for direct orbital perturbations. Moreover, global ocean tide models are of interest in the study of energy dissipation in the earth-moon system and, for oceanographic studies, the global ocean tidal currents are of interest.

The dynamics of the global ocean tides are described by the nonlinear Laplace Tidal Partial Differential Equations. The equations are too complex to solve analytically, and are amenable only to numerical solution by computer. In a previous work (Estes [9]) which we will refer to as report [A], a computer software system was developed to solve for theoretical global tides described by the Laplace Tidal Equations (LTE) including static earth tides, bottom friction and turbulent viscosity. Following Zahel [25], a time stepping integration technique incorporating impermeable coastal boundary conditions and a forward time difference/central spatial difference numerical scheme was used. The present development is an extension of that work to include ocean self-gravitation and crustal loading effects into the Laplace Tidal Equations. As discussed by Hendershott [15], the inclusion of these effects forces the LTE into an integro-differential system which we denote by IDLTE (Integro - Differential Laplace Tidal Equation). For purposes of completeness, much of the material of report [A] will be repeated, particularly in the development of the tidal equations and in the description of the software system design.

Report [A] presented numerical solutions of LTE for the M_2 and K_1 tidal constituents. We have since obtained solutions for S_2 , N_2 , K_2 , O_1 and P_1 . For convenience of reference, we include a complete set of these theoretical solutions, which show general agreement with empirical global solutions with respect to the positions of amphidromic systems and tidal amplitudes. An M_2 solution of IDLTE (i.e., including ocean self-gravitation and crustal loading) has been generated and displays a marked improvement in the predicted phase relations with observations (generally within 30°) when compared to the LTE M_2 solution. IDLTE solutions for additional constituents will be generated

and presented in a future publication.

The improved comparison with observations obtained from the theoretical M_2 solution with the inclusion of self-gravitation and crustal loading effects are encouraging. However, the observed values of ocean tides contain meteorological effects and effects from terms beyond the second order term of the astronomical tidal potential which are neglected in the theoretical models. Moreover, the representation of the eddy viscosity deserves further study, as well as internal waves, tide currents and long period ocean tides which are not considered in the present study. In addition, the parameters representing the earth model (Love numbers and load Love numbers) are averaged quantities so that local responses of the earth due to inhomogeneities are not included. These effects must be correctly modeled before agreement to the 10 centimeter level can be achieved.

2.0 LAPLACE TIDAL EQUATIONS

The dynamic equations which describe the ocean tides, first derived by Laplace (1775), are

$$\begin{aligned}
 \frac{\partial u}{\partial t} - 2\omega \sin\phi v &= \frac{-g}{R \cos\phi} \frac{\partial}{\partial \lambda} [\xi_s] + F_\lambda \\
 \frac{\partial v}{\partial t} + 2\omega \sin\phi u &= -\frac{g}{R} \frac{\partial}{\partial \phi} [\xi_s] + F_\phi \\
 \frac{\partial \xi}{\partial t} &= -\frac{1}{R \cos\phi} \left[\frac{\partial}{\partial \lambda} (Hu) + \frac{\partial}{\partial \phi} (Hv \cos\phi) \right] \\
 H &= h(\phi, \lambda) + \xi_s - \xi_b
 \end{aligned} \tag{1}$$

The first two equations are essentially a linearized special case of the Navier-Stokes equations and the third is a continuity mass conservation equation. Here ϕ denotes latitude, λ longitude, u the eastward component of velocity, v the northward component of velocity, F_λ and F_ϕ the components of the tidal force, g the gravity acceleration, R the mean earth radius, and ω the rotational velocity of the Earth. The ocean depth $h(\phi, \lambda)$ denotes that distance from the water surface to the ocean bottom when averaged over a very long time period

$$h(\phi, \lambda) = \lim_{T \rightarrow \infty} \frac{1}{T} \int_0^T h(\phi, \lambda, t) dt$$

and $\xi_s(\phi, \lambda, t)$, $\xi_b(\phi, \lambda, t)$ denote the instantaneous elevations of the ocean surface and ocean bottom above their time averaged values. Thus the instantaneous upward displacement of the ocean surface relative to the ocean bottom, the quantity measured by tidal gauges, is given by (see Figure 1)

$$\begin{aligned}
 \xi(\phi, \lambda, t) &= h(\phi, \lambda, t) - h(\phi, \lambda) \\
 &= \xi_s(\phi, \lambda, t) - \xi_b(\phi, \lambda, t)
 \end{aligned} \tag{2}$$

These equations are referred to as "long-wave" equations. In their derivation the ocean is regarded as a homogeneous and incompressible fluid, and nonlinear acceleration terms are neglected as second order effects. The assumption of hydrostatic equilibrium is invoked in deriving the continuity equation, in that it makes the horizontal velocity components independent of

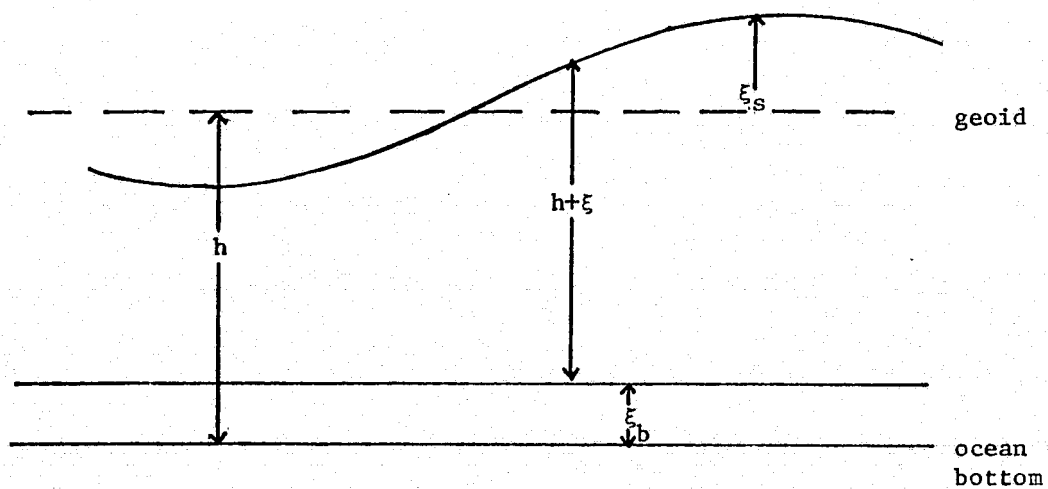


Figure 1

the radial direction and allows integration of the expression for the balance of mass in a vertical water column from the ocean floor to the ocean surface. The vertical velocity W need not be considered explicitly, as the Coriolis term $\omega \cos \phi W$ is neglected in the first equation for the eastward velocity component.

The displacements of the ocean and solid earth in response to \bar{T} , the direct tidal forces due to the moon and sun, results in an altered mass distribution due to the formation of the tidal bulge inside the Earth and hence a change in the Earth's gravitational field. Let \bar{F}_b and \bar{F}_s denote the gravitational disturbances of the bodily tide and ocean tide, respectively. Moreover, denote the forces of friction and lateral turbulent viscosity by \bar{F}_f and \bar{F}_v . Then

$$\bar{F} = \bar{T} + \bar{F}_b + \bar{F}_s + \bar{F}_f + \bar{F}_v . \quad (3)$$

The direct tidal force, \bar{T} , can be expressed as the gradient of the tidal potential Γ ,

$$\bar{T} = \nabla \Gamma \quad (4)$$

The gravitational disturbance due to the bodily tide results from two sources; a primary response to the non-loading astronomical potential and a secondary response to the crustal loading by the time varying ocean tide. The Green's functions for the augmented potential and elevation caused by the loading of the crust at an angular distance γ (spherical earth) per unit of loading mass are given by Farrell [10] as

$$\begin{aligned} \phi'(\gamma) &= \frac{Rg}{M_e} \sum_{n=0}^{\infty} k'_n P_n(\cos \gamma) \\ U'(\gamma) &= \frac{R}{M_e} \sum_{n=0}^{\infty} h'_n P_n(\cos \gamma) \end{aligned} \quad (5)$$

where M_e is the mass of the earth and k'_n , h'_n are load Love numbers. The primary solid earth tide, due to the fact that the free periods of the elastic earth vibration are less than an hour, is accurately represented as a static response. Thus the total body elevation and gravitational disturbance are

$$\xi_b = \frac{h_L}{g} \Gamma + \iint_{\Omega} R^2 \xi_{\rho} U'(\gamma) d\Omega' \quad (6)$$

$$\bar{F}_b = k_L \bar{T} + \nabla v_b \quad (7)$$

where

$$v_b = \iint_{\Omega} R^2 \xi_{\rho} \Phi'(\gamma) d\Omega' \quad (8)$$

Here ρ is the mean density of sea-water, the domain of integration is over the global ocean surface and γ is the angle between the integration variable and the position at which the integrals are being evaluated,

$$\cos \gamma = \sin \phi \sin \phi' + \cos \phi \cos \phi' \cos(\lambda - \lambda'). \quad (9)$$

The first terms (static) in the equations for ξ_b and \bar{F}_b are expressed in terms of the Love numbers k_L and h_L with values of approximately .3 and .6, respectively. These parameters express the elastic yielding of the Earth to a non-loading potential. The gravitational disturbance of the ocean tide is

$$\bar{F}_s = \nabla V_s \quad (10)$$

where

$$V_s = \iint_{\Omega} \frac{G \rho R^2 \xi d\Omega'}{|\bar{x} - \bar{x}'|} \quad (11)$$

and the domain of integration is over the ocean surface. Here G is the gravitational constant and \bar{x} , \bar{x}' represent the position on the earth's surface at which \bar{F}_s is evaluated and the position of the element of integration, respectively. On the surface of the spherical earth,

$$|\bar{x} - \bar{x}'| = \sqrt{2R^2(1 - \cos \gamma)}$$

so that

$$\begin{aligned}
 v_s &= \iint_{\Omega} \frac{G \rho R^2 \xi}{2R \sin(\gamma/2)} d\Omega' \\
 &= \iint_{\Omega} R^2 \xi \rho \frac{Rg}{M_e} \frac{d\Omega'}{2 \sin(\gamma/2)} \quad (12)
 \end{aligned}$$

In modeling the friction and lateral viscosity terms we follow Zahel [25] and set

$$\begin{aligned}
 \bar{F}_f &= \frac{C_r \sqrt{u^2 + v^2}}{H} \begin{pmatrix} u \\ v \end{pmatrix} \\
 \bar{F}_v &= C_{hv} \Delta \begin{pmatrix} u \\ v \end{pmatrix} \quad (13)
 \end{aligned}$$

where C_r and C_{hv} are the coefficients of friction and horizontal eddy viscosity, respectively, and Δ is the horizontal Laplacian

$$\Delta \equiv \frac{1}{R^2 \cos^2 \phi} \frac{\partial^2}{\partial \lambda^2} + \frac{1}{R^2} \frac{\partial^2}{\partial \phi^2} .$$

The Laplace tidal equations thus becomes

$$\begin{aligned}
 \frac{\partial u}{\partial t} - 2\omega \sin \phi v &= \frac{(1+k_L - h_L)}{R \cos \phi} \frac{\partial \Gamma}{\partial \lambda} - \frac{g}{R \cos \phi} \frac{\partial \xi}{\partial \lambda} - C_r \frac{\sqrt{u^2 + v^2}}{H} u + C_{hv} \Delta u + \frac{1}{R \cos \phi} \frac{\partial \Gamma'}{\partial \lambda} \\
 \frac{\partial v}{\partial t} + 2\omega \sin \phi u &= \frac{(1+k_L - h_L)}{R} \frac{\partial \Gamma}{\partial \phi} - \frac{g}{R} \frac{\partial \xi}{\partial \phi} - C_r \frac{\sqrt{u^2 + v^2}}{H} v + C_{hv} \Delta v + \frac{1}{R} \frac{\partial \Gamma'}{\partial \phi} \quad (14) \\
 \frac{\partial \xi}{\partial t} + \frac{1}{R \cos \phi} \left[\frac{\partial (Hu)}{\partial \lambda} + \frac{\partial (Hv \cos \phi)}{\partial \phi} \right] &= 0
 \end{aligned}$$

where

$$H = h(\phi, \lambda) + \xi$$

and Γ' is the potential due to ocean loading and self-gravitational effects,

$$\Gamma'(\phi, \lambda, t) = \iint_{\Omega} R^2 \xi(\phi', \lambda', t) \rho \left[\frac{Rg}{M_e} \frac{1}{2\sin(\gamma/2)} + \Phi'(\gamma) - g U'(\gamma) \right] d\Omega' \quad (15)$$

$$\cos \gamma = \sin \phi \sin \phi' + \cos \phi \cos \phi' \cos(\lambda - \lambda')$$

The LTE thus becomes integro-differential in nature (IDLTE) when ocean loading and self-gravitation effects are included, as pointed out by Hendershott [15]. Neglecting the perturbing potential Γ' reduces the system to that of report A. The present study solves the IDLTE system by successive approximations using the time stepping method of Hansen [12] and finite differences, imposing the boundary conditions of impermeable coasts, i.e., the perpendicular components of tidal velocity are required to vanish at the coasts. The procedure is to first generate a zeroth order solution of Equation (14) neglecting Γ' . Then Γ' is calculated from Equation (15) using the zeroth order solution for the tide ξ . A first order solution of Equation (14) is then generated using the potential Γ' calculated from the zeroth order solution, etc. This successive iteration technique is continued until convergence is achieved.

The periodic tidal solution is represented in the form

$$\xi(\phi', \lambda', t) = A(\phi', \lambda') \cos[\sigma t + \Psi(\phi', \lambda')] \quad (16)$$

where contours of equal amplitude $A(\phi', \lambda')$ are denoted corange lines and lines of constant phase Ψ are denoted cotidal lines. The expression for Γ' then becomes

$$\Gamma'(\phi, \lambda, t) = P(\phi, \lambda) \cos \sigma t - Q(\phi, \lambda) \sin \sigma t \quad (17)$$

where

$$P(\phi, \lambda) = \iint_{\Omega} R^2 \rho A(\phi', \lambda') \cos[\Psi(\phi', \lambda')] \left[\frac{Rg}{M_e} \frac{1}{2\sin(\gamma/2)} + \Phi'(\gamma) - g U'(\gamma) \right] \sin \phi' d\phi' d\lambda' \quad (18)$$

$$Q(\phi, \lambda) = \iint_{\Omega} R^2 \rho A(\phi', \lambda') \sin[\psi(\phi', \lambda')] \left[\frac{Rg}{M_e} \frac{1}{2\sin(\gamma/2)} + \phi'(\gamma) - gU'(\gamma) \right] \sin\phi' d\phi' d\lambda'$$

Then

$$\begin{aligned} \frac{\partial \Gamma'}{\partial \lambda} &= \frac{\partial P}{\partial \lambda} \cos\sigma t - \frac{\partial Q}{\partial \lambda} \sin\sigma t \\ \frac{\partial \Gamma'}{\partial \phi} &= \frac{\partial P}{\partial \phi} \cos\sigma t - \frac{\partial Q}{\partial \phi} \sin\sigma t \end{aligned} \quad (19)$$

3.0 TIDAL POTENTIAL EXPANSION

The complex motion of the moon and sun results in a tidal disturbing force which displays periods ranging from thousands of years to hours. Doodson [7] and recently Cartwright [4] have expanded the gravitational potential of the moon and sun at a point on the Earth's surface into the series of tidal "components" or "constituents"

$$V(\phi, \lambda, t) = \sum_{n_1, n_2, \dots, n_6} \beta(n_1, n_2, \dots, n_6) \exp i(n_1 \tau + n_2 s + \dots + n_6 p_s) \quad (20)$$

where the sum is over all positive and negative values of the integers n_i . The arguments of the exponential are the six astronomical frequencies presented in Table I. The number

$$(n_1, n_2+5, n_3+5, n_4+5, n_5+5, n_6+5) \quad (21)$$

is known as the Doodson number and uniquely identifies individual components.

The functions ϕ are grouped into three species, for $n_1 = 0, 1$, and 2 . The functional forms are

SPECIES I:

$$\beta(0, \dots, n_6) = g_{CKP}_2(\sin \phi)$$

SPECIES II:

$$\beta(1, \dots, n_6) = g_{CKP}_2^1(\sin \phi) e^{+i\lambda} \quad (22)$$

SPECIES III:

$$\beta(2, \dots, n_6) = g_{CKP}_2^2(\sin \phi) e^{+2i\lambda}$$

The $C(n_2, n_3, \dots, n_6)$ are constants, the P_n^m are Legendre polynomials and

$$K = \frac{3}{2} \left(\frac{M_{\text{moon}}}{M_e} \right) \frac{R^4}{R_{\text{moon}}^3} = 53.7 \text{ cm} \quad (23)$$

where R_{moon} denotes the mean lunar distance.

The fictitious displacement

$$\bar{\xi}(t) = \frac{\beta(n_1, \dots, n_6)}{g} \quad (24)$$

is denoted the "equilibrium tide" and represents a sea surface of constant gravitational potential. The tidal constituent potential is then $\Gamma = g\bar{\xi}$.

From the definition of τ , it is clear that Species III tides are semidiurnal, Species II diurnal, and Species I long period tides. Doodson computed the constituents with amplitude greater than 10^{-4} of the amplitude of the largest tide, some 400 terms. The most prominent terms are presented in Table II.

For the present study, long period tides are not considered and for input purposes to the computer program, the tidal constituents are represented in the form

TYPE III:

$$\bar{\xi} = \frac{\bar{CK}}{2} \cos^2 \phi e^{i(\sigma t + 2\lambda)} \quad (25)$$

TYPE II:

$$\bar{\xi} = \bar{CK} \sin 2\phi e^{i(\sigma t + \lambda)}$$

where the constants \bar{C} and σ are specified by the particular constituent of interest, and

$$\sigma = n_1 \dot{t} + n_2 \dot{s} + n_3 \dot{h} + n_4 \dot{p} + n_5 \dot{N} + n_6 \dot{p}_s \quad (26)$$

where the rate of change is per mean solar hour. Note the factor of 2 difference in the semidiurnal and diurnal representation of Equation (25).

	Definition	Period	Rate (radians per mean solar hour)	Frequency (deg/solar hour)
γ	Greenwich celestial longitude	1 lunar day	.2529359	14.492
s	Lunar orbital longitude	1 tropical month	.0095819	.549016
h	Solar orbital longitude	1 tropical year	.007163	.041068
p	Lunar perigee longitude	8.85 Julian years	.00008168	.004642
N	Lunar node longitude	18.61 Julian years	.0000377	-.002206
P_s	Solar perigee longitude	20,900 Julian years	$.344 \times 10^{-7}$.00000196

Table I

<u>Darwin</u>	<u>Designation</u> <u>Doodson Number</u>	<u>Amplitude Factor</u> <u>(C)</u>	<u>Frequency</u> <u>(radians/day)</u>	<u>Period</u> <u>(Hours)</u>
Type I				
M _f	(0,7,5,5,5,5)	.156	.459969	327.84
Type II				
O ₁	(1,4,5,5,5,5)	.377	5.840445	25.82
P ₁	(1,6,3,5,5,5)	.176	6.265983	24.07
K ₁	(1,6,5,5,5,5)	.531	6.300388	23.93
Type III				
N ₂	(2,4,5,6,5,5)	.174	11.910864	12.66
M ₂	(2,5,5,5,5,5)	.908	12.140833	12.42
S ₂	(2,7,3,5,5,5)	.423	12.56637061	12.00
K ₂	(2,7,5,5,5,5)	.115	12.600776	11.97

Table II

4.0 COMPUTATIONAL TECHNIQUES

4.1 Hansen Grid

The numerical technique employed in the present study for the Laplace Tidal Equations (14) follows Hansen [12] and Zahel [25] in applying a finite difference algorithm in temporal and spatial variables and integrating forward in time (timestepping). We employ the global grid system proposed by Hansen (also known as the Richardson grid) whereby a staggered grid with velocity components and tidal elevations are computed at adjacent, but not coincident, grid points. The coastal boundary conditions are represented by horizontal and vertical lines imposed on the grid and pass only through those points denoting velocity components. Vertical boundary lines pass through u grid points (eastward velocity) and horizontal boundary lines pass through v grid points (northward velocity) so that the requirement of the vanishing of perpendicular components of velocity forces all velocity components falling on the boundary line to be identically zero for all time. Moreover, it is to be noted that with this procedure there is never a corner point involved in the boundary conditions. This is of considerable numerical importance. The Hansen grid is depicted in Figure 2.

4.2 Finite Difference Equations

The finite difference formulation for the Laplace Tidal Equations (14), using central differences for spatial variables and forward differences for the time variable are, following Zahel [25]

$$\begin{aligned}
 & u(N, M, t_{n+1}) \\
 &= \left\{ 1 - \frac{C_F \Delta t \sqrt{u(N, M, t_n)^2 + \frac{1}{16} [v(N, M-1, t_n) + v(N, M, t_n) + v(N+1, M-1, t_n) + v(N+1, M, t_n)]^2}}{\frac{1}{2} [h(N, M) + h(N, M-1) + \xi(N, M, t_n) + \xi(N, M-1, t_n)]} \right\} \\
 & \cdot u(N, M, t_n) + 2\omega \Delta t \sin[\phi(N)] \\
 & \cdot \frac{1}{4} [v(N, M-1, t_n) + v(N, M, t_n) + v(N+1, M-1, t_n) + v(N+1, M, t_n)] \\
 & + C_{hv} \frac{\Delta t}{v} \left\{ \frac{u(N, M-1, t_n) + u(N, M+1, t_n) - 2u(N, M, t_n)}{[R \cos[\phi(N)] \Delta \lambda]^2} \right. \\
 & \left. + \frac{u(N+1, M, t_n) + u(N-1, M, t_n) - 2u(N, M, t_n)}{[R \Delta \phi]^2} \right\}
 \end{aligned}$$

$$- \frac{g\Delta t}{R\cos[\phi(N)]} \frac{\xi(N,M,t_n) - \xi(N,M-1,t_n)}{\Delta\lambda} + \frac{\Delta t}{R\cos[\phi(N)]} \left\{ \frac{\partial P}{\partial\lambda}(N,M)\cos[\sigma t_n] - \frac{\partial Q}{\partial\lambda}(N,M)\sin[\sigma t_n] \right\}$$

$$+ F_\lambda \Delta t$$

$$v(N,M,t_n)$$

$$= \left\{ 1 - \frac{C_F \Delta t \sqrt{v(N,M,t_n)^2 + \frac{1}{16}[u(N-1,M,t_n) + u(N-1,M+1,t_n) + u(N,M+1,t_n) + u(N,M,t_n)]^2}}{\frac{1}{2}[h(N,M) + h(N-1,M) + \xi(N,M,t_n) + \xi(N-1,M,t_n)]} \right\}$$

$$\cdot v(N,M,t_n) - 2\omega\Delta t \sin[\phi(N) - \frac{\Delta\phi}{2}]$$

$$\cdot \frac{1}{4}[u(N-1,M,t_n) + u(N-1,M+1,t_n) + u(N,M+1,t_n) + u(N,M,t_n)]$$

$$+ C_{hv} \Delta t \left\{ \frac{v(N,M-1,t_n) + v(N,M+1,t_n) - 2v(N,M,t_n)}{[R\cos[\phi(N) - \frac{\Delta\phi}{2}]\Delta\lambda]^2} \right. \quad (27)$$

$$+ \left. \frac{v(N+1,M,t_n) + v(N-1,M,t_n) - 2v(N,M,t_n)}{[R\Delta\phi]^2} \right\}$$

$$- \frac{g\Delta t}{R} \left\{ \frac{\xi(N,M,t_n) - \xi(N-1,M,t_n)}{\Delta\phi} \right\} + \frac{\Delta t}{R} \left\{ \frac{\partial P}{\partial\phi}(N,M)\cos[\sigma t_n] - \frac{\partial Q}{\partial\phi}(N,M)\sin[\sigma t_n] \right\}$$

$$+ F_\phi \Delta t$$

where

$$\frac{\partial P}{\partial\lambda}(N,M) = \frac{P(N,M) - P(N,M-1)}{\Delta\lambda}$$

$$\frac{\partial Q}{\partial\lambda}(N,M) = \frac{Q(N,M) - Q(N,M-1)}{\Delta\lambda}$$

$$\frac{\partial P}{\partial\phi}(N,M) = \frac{P(N,M) - P(N-1,M)}{\Delta\phi}$$

$$\frac{\partial Q}{\partial\phi}(N,M) = \frac{Q(N,M) - Q(N-1,M)}{\Delta\phi}$$

(28)

where

$$F_{\lambda} = \frac{g}{R \cos \phi} \frac{\partial \bar{\xi}}{\partial \lambda}$$

$$F_{\phi} = \frac{g}{R} \frac{\partial \bar{\xi}}{\partial \phi}$$

and

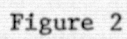
$$\text{SPECIES III: } \begin{cases} F_{\lambda} = -\frac{CgK}{R} \cos [\phi(N)] \sin [2(\lambda(M) - \frac{\Delta\lambda}{2}) + \sigma t_n] \\ F_{\phi} = -\frac{CgK}{2R} \sin [2(\phi(N) - \frac{\Delta\phi}{2})] \cos [2\lambda(M) + \sigma t_n] \end{cases}$$

$$\text{SPECIES II: } \begin{cases} F_{\lambda} = -\frac{2CgK}{R} \sin [\phi(N)] \sin [(\lambda(M) - \frac{\Delta\lambda}{2}) + \sigma t_n] \\ F_{\phi} = \frac{2CgK}{R} \cos [2(\phi(N) - \frac{\Delta\phi}{2})] \cos [\lambda(M) + \sigma t_n] \end{cases} \quad (29)$$

The quantities $\frac{\partial P}{\partial \lambda}$, $\frac{\partial Q}{\partial \lambda}$, $\frac{\partial P}{\partial \phi}$, and $\frac{\partial Q}{\partial \phi}$ arise from the perturbing potential Γ' and are held constant in time over an iteration (see Section 2.0). For computing efficiency these derivatives are precalculated and held in storage for the integration algorithm. The continuity equation becomes

$$\xi(N, M, t_{n+1}) = \xi(N, M, t_n)$$

$$\begin{aligned} & + \frac{\Delta t}{R \cos [\phi(N)]} \left\{ \frac{\frac{1}{2}[h(N, M) + h(N, M-1) + \xi(N, M, t_n) + \xi(N, M-1, t_n)] u(N, M, t_{n+1})}{\Delta \lambda} \right. \\ & - \frac{\frac{1}{2}[h(N, M+1) + h(N, M) + \xi(N, M+1, t_n) + \xi(N, M, t_n)] u(N, M+1, t_{n+1})}{\Delta \lambda} \\ & + \frac{\frac{1}{2}[h(N, M) + h(N-1, M) + \xi(N, M, t_n) + \xi(N-1, M, t_n)] v(N, M, t_{n+1})}{\Delta \lambda / \cos [\phi(N) - \frac{\Delta \phi}{2}]} \\ & \left. - \frac{\frac{1}{2}[h(N+1, M) + h(N, M) + \xi(N+1, M, t_n) + \xi(N, M, t_n)] v(N+1, M, t_{n+1})}{\Delta \phi / \cos [\phi(N+1) - \frac{\Delta \phi}{2}]} \right\} \end{aligned} \quad (30)$$



It is to be noted that the tidal elevation ξ at time t_{n+1} is calculated in terms of the velocities at time t_{n+1} . The finite difference formulas for the velocities u and v involve only nearest neighbor points, with the exception of the Laplacian terms for turbulent viscosity. For grid points adjacent to coastal boundaries, the evaluation of the Laplacian central difference term involves a grid point which would fall on land. The computer algorithm handles this by assuming the normal derivative of velocity at the boundary to vanish, thereby eliminating the need to evaluate the point. In this way values at land grid points are never involved in the algorithm. (Coastal boundary points are not considered to be land points.) Note that these Laplacian terms are small relative to the other terms, having an R^2 divisor.

4.3 Stability

The stability of the system described by Equation (14) neglecting the Γ' terms has been discussed in Report A. In particular, it was shown that the global tides computed by the time stepping procedure become periodic in time and independent of the initial state (providing the initial values of u, v, ξ were small enough that the system did not immediately blow up) within five tidal periods, provided the time step Δt is small enough to insure stability. The strong dissipation of the friction and lateral viscosity terms are the cause of this rapid convergence, quickly damping out the initial transients in the numerical integration and eliminating spurious waves. A stability analysis for Equations (14) less the Γ' terms has been performed by Zahel [25] where formulas for the maximum time step Δt_{\max} as a function of grid spacing, latitude limits and dissipation parameters C_r and C_{hv} are given which will guarantee stability for the tidal solution. Report A describes a numerical procedure for easily establishing a suitable time step.

The successive approximation method proposed in Section 2.0 presents no difficulty in establishing a Δt_{\max} for a given iteration to insure stability, as the Γ' terms on the right hand side of Equations (14) are known functions of position and time. The conditions under which a successive approximation procedure will converge to the solution of the integro-differential system described by Equations (14) for the perturbing potential Γ' will not be pursued in this report.

4.4 Integration Algorithm and Solution Representation

The program implementation of the integration algorithm for Equations (14) and their boundary conditions is briefly described in Report A. The basic design is such that calculations are performed on a single latitude band at a time and required quantities are accumulated over three bands. The computer code features compact arrays for all variables u, v, ξ and h with values only at non-boundary ocean points on the global grid. Compact arrays also exist for $\frac{\partial P}{\partial \lambda}, \frac{\partial P}{\partial \phi}, \frac{\partial Q}{\partial \lambda}, \frac{\partial Q}{\partial \phi}$. The precalculation of the derivatives of P and Q increases the core requirements of the program, but results in a substantial savings of CPU time. All variables required by the integration algorithm reside in core which helps keep I/O and CPU time requirements down. The time needed to integrate Equations (14) on a global $3^\circ \times 3^\circ$ grid with a 3 minute step size for 12 hours is approximately 3 CPU minutes on an IBM 360/91. Thus, to integrate over 6 periods of a semi-diurnal tide requires approximately 20 CPU minutes. The CPU time increases substantially for finer global grid meshes (and consequently smaller time steps).

The program is designed with an overlay structure to minimize computer core storage requirements. A solution with a global grid resolution of $3^\circ \times 3^\circ$ can be accommodated in under 500K bytes of core. A $2^\circ \times 2^\circ$ global grid requires approximately 600K bytes of core, while a global $1^\circ \times 1^\circ$ grid would need slightly in excess of 1000K bytes.

The tidal solution $\xi(\phi, \lambda; t)$ obtained by the software system in time-stepping from time $t=0$ to $t=T$ is specified on the global grid at time $t = T$. It is convenient (and conventional) to represent the periodic solution in the form (Equation (16))

$$\xi(\phi, \lambda; t) = A(\phi, \lambda) \cos [\Psi(\phi, \lambda) + \sigma t]$$

where t is expressed in mean solar time. The computer software establishes this representation by integrating the solution over a quarter of a tidal period from $t = T$ to $t = T + \pi/2\sigma$ so that

$$\begin{aligned} A(\phi, \lambda) &= \sqrt{\xi(\phi, \lambda; T)^2 + \xi(\phi, \lambda; T + \pi/2\sigma)^2} \\ \Psi(\phi, \lambda) &= \tan^{-1} \left[\frac{-\xi(\phi, \lambda; T + \pi/2\sigma)}{\xi(\phi, \lambda; T)} \right] - \sigma T \end{aligned} \quad (31)$$

The software system employs a graphics package to display solutions in terms of corange lines (contours of equal amplitude $A(\phi, \lambda)$) and cotidal lines (lines of equal phase $\Psi(\phi, \lambda)$). For purposes of display, we employ the representation

$$\xi(\phi, \lambda; t) = A(\phi, \lambda) \cos[\sigma t - S(\phi, \lambda)] \quad (32)$$

where

$$S(\phi, \lambda) = -\Psi(\phi, \lambda) \quad (33)$$

The cotidal values appearing on the tidal charts presented in this report are expressed in hours 0 to 24, instead of angular measurement. Hour values are obtained by dividing the phase function S expressed in degrees by 15 degrees per solar hour. Note that both diurnal and semi-diurnal tides have cotidal values expressed in hours from 0 to 24. These relationships are given explicitly as

$\Psi(\text{degrees})$	0	330	300	270	240	210	180	150	120	90	60	30
$S(\text{degrees})$	0	30	60	90	120	150	180	210	240	270	300	330
$S(\text{hours})$	0	2	4	6	8	10	12	14	16	18	20	22

4.5 Evaluation of Green's Functions for Ocean Loading

The Green's functions for the augmented potential and elevation caused by the loading of the crust given by Equations (5) are slowly converging series, as discussed by Farrell [10]. Following Farrell, and using the identities

$$\sum_{n=0}^{\infty} P_n(\cos \gamma) = \frac{1}{2\sin(\gamma/2)} \quad (34)$$

$$\sum_{n=0}^{\infty} \frac{P_n(\cos \gamma)}{n} = -\ln \left\{ 2\sin(\gamma/2) [1 + \sin(\gamma/2)] \right\}$$

we rewrite Equations (5) in the form

$$\begin{aligned} U'(\gamma) &= \frac{R}{M_e} \left\{ \sum_{n=0}^{\infty} (h'_n - h_{\infty}) P_n(\cos \gamma) + h_{\infty} \sum_{n=0}^{\infty} P_n(\cos \gamma) \right\} \\ &= \frac{R}{M_e} \left\{ \frac{h_{\infty}}{2\sin(\gamma/2)} + \sum_{n=0}^{\infty} (h'_n - h_{\infty}) P_n(\cos \gamma) \right\} \end{aligned} \quad (35)$$

$$\begin{aligned} \Phi'(\gamma) &= \frac{Rg}{M_e} \left\{ \sum_{n=0}^{\infty} \left(\frac{nk'_n - k_{\infty}}{n} \right) P_n(\cos \gamma) + k_{\infty} \sum_{n=1}^{\infty} \frac{P_n(\cos \gamma)}{n} \right\} \\ &= \frac{Rg}{M_e} \left\{ \sum_{n=1}^{\infty} \frac{nk'_n - k_{\infty}}{n} P_n(\cos \gamma) - k_{\infty} \ln [2\sin(\gamma/2) [1 + \sin(\gamma/2)]] \right\} \end{aligned}$$

where

$$\begin{aligned} h_{\infty} &= \lim_{n \rightarrow \infty} h'_n \\ k_{\infty} &= \lim_{n \rightarrow \infty} nk'_n \end{aligned} \quad (36)$$

We have investigated several summation techniques for evaluating the series in Equation (35), including the Shanks convergence acceleration method [23].

However, we found the Euler transformation method discussed by Farrell to be the most efficient. The values of k'_n and h'_n used are those given by Farrell for the G-B Earth Model, where

$$k_\infty = - 2.482$$

$$h_\infty = - 5.005$$

Moreover, we have used the value

$$h_0 = - .134$$

obtained by Longman [19] for a Gutenberg Earth Model. Farrell gives values of h'_n, k'_n for

$$n = 1, 2, 3, 4, 5, 6, 8, 10, 18, 32, 56, 100, 180, 325, 550, 1000, 1800, 3000, 10000.$$

Quadratic polynomials were fitted through these values to obtain k'_n, h'_n for other values of n required for the summations.

Table III presents calculated values for $U'(\gamma), \Phi'(\gamma)$ and the Greens function

$$R^2 \rho \left[\frac{Rg}{M_e} \frac{1}{2\sin(\gamma/2)} + \Phi'(\gamma) - gU'(\gamma) \right] \quad (37)$$

For convenience of comparison, the values of U' and Φ' are scaled by $(R\gamma) \times 10^{12}$, with γ in radians. The quantities are in mks units, and an applied load of 1 kg. is assumed. Values taken for R, ρ, g and M_e are 6371000., 1030., 9.82, and 5.975×10^{24} , respectively.

TABLE III

degrees	$U'(\gamma) \times R \times \gamma \times 10^{12}$	$\Phi'(\gamma) \times R \times \gamma \times 10^{12}$	Green's Function (m ² /sec ² kg)
1°	-13.196	-1.663	73.178
2°	- 9.725	-1.159	30.277
3°	- 7.490	-0.025	17.576
4°	- 6.028	1.368	11.964
5°	- 5.294	2.886	9.144
6°	- 4.625	4.494	7.310
7°	- 4.164	6.158	6.112
8°	- 3.971	7.850	5.339
9°	- 3.921	9.580	4.798
10°	- 3.718	11.367	4.311
20°	- 2.603	31.214	2.328
30°	- 1.577	53.987	1.716
40°	- 0.293	78.671	1.406
50°	0.838	104.017	1.238
60°	1.674	128.809	1.142
70°	2.076	152.136	1.089
80°	2.047	173.445	1.061
90°	1.647	192.523	1.046
100°	0.924	209.427	1.039
110°	- 0.029	224.447	1.035
120°	- 1.138	238.011	1.033
130°	- 2.311	250.661	1.032
140°	- 3.439	262.991	1.030
150°	- 4.506	275.579	1.028
160°	- 5.438	288.956	1.027
170°	- 6.263	303.668	1.027
180°	- 6.660	320.324	1.025

4.6 Tidal Solutions Neglecting Loading and Self-Gravitation Effects

Solutions for the principal tidal constituents M_2 , S_2 , N_2 , K_2 , K_1 , O_1 and P_1 have been generated using the integration algorithm described in Section 4.1 neglecting the terms involving Γ' and are displayed in Figures 3-9. These tide models are then solutions of the LTE as described in Report A, and do not exhibit an integro-differential character (IDLTE). They would, however, serve as the initial approximations for the successive approximation algorithm described in Section 2.0 for the IDTLE (see Section 4.7). Global grid resolutions of both $3^\circ \times 3^\circ$ and $2^\circ \times 2^\circ$ have been used for generating tide models for the principal constituents and display excellent agreement. The Love parameter values used in these solutions were $k_L = .3$ and $h_L = .6$ while the dissipation parameters were $C_r = .003$ and $C_{hv} = 10^7$, respectively (the same values used by Zahel [25, 26]). In the $2^\circ \times 2^\circ$ numerical models the effects of the tides of polar seas north of 80° latitude are ignored (81° latitude for the $3^\circ \times 3^\circ$ models). This is due to the fact that increasing the northern latitude limit necessitates decreasing the integration step size to maintain stability, hence greatly increasing the computer time needed to arrive at the solution. However, our numerical experimentation has shown that increasing the northern latitude limit has no discernable impact on the solution south of 80° . The ocean depth profile used in the solutions is presented in Figure 10. Initial values of u , v and ξ at time $t = 0$ were set to zero. A time series plot of the M_2 tidal solution, ξ , for a grid point in the central Atlantic is presented in Figure 11. The solution grows from the zero initial solution to a steady state solution within several periods. All solutions for the principal constituents presented in this section were integrated over eight tidal periods (assuring a steady state solution) before the amplitudes and phases (Equation (31)) were calculated.

Prominent features evident in both the diurnal and semi-diurnal solutions are amphidromic systems, or geographic regions where the tidal amplitude vanishes. Cotidal lines radiate from the amphidromic points, where the sense of the amphidromic system is denoted as the direction in which the high tide occurs progressively later. Amphidromes are usually (not always) counter-clockwise in the Northern Hemisphere and clockwise in the Southern Hemisphere. These stationary centers can result physically as a consequence of the characteristic wave velocity being of the same order of magnitude of the velocity of the sublunar point.

The family of semi-diurnal waves M_2 , S_2 , N_2 , K_2 exhibits very similar characteristics in the tidal solutions, as does the family K_1 , O_1 , P_1 of diurnal waves. For this reason we will only discuss the M_2 and K_1 solutions of Figures 3 and 7 in detail.

The M_2 solution of Figure 3 was compared with the numerical solutions of Hendershott [15], Pekeris and Accad [21], Zahel [25], and Bogdanov and Magarik [3] as to tidal amplitude, phases and location of amphidromic systems. These solutions are conveniently summarized by Hendershott [14]. Our M_2 solution compares very closely with Zahel, with nearly a systematic 30% decrease in tidal amplitudes consistent with the factor $(1+k_2-h_2)$ in our solution. The various models are in fairly good agreement in the North and South Atlantic, with the exception that Hendershott does not find the South Atlantic amphidrome, and the amphidrome at the southern tip of South America is farther west in ours and Zahel's solution relative to the dissipative model of Pekeris. All models are again quite similar in the Indian Ocean, being dominated by a large "antiamphidrome", i.e. a region of high tidal amplitude moving nearly synchronously. The amplitude of this feature shown by Hendershott is substantially larger than the other models. Our experimentation shows that the region at the southern tip of Madagascar is near an amphidromic state. The Pacific basin shows the greatest differences between the numerical models. Our solution, along with Zahel, shows the appearance of an amphidromic system off of California, and a line of rapid phase change in a concave arc running from Central America to Southern Peru. Our model, in agreement with Zahel, shows two antiamphidromes on either side of the dominant South Central Pacific amphidrome, although the eastern antiamphidrome of our model is more pronounced than that of Zahel. The Western Pacific basin does not show the pseudo-nodal line extending from Japan to New Guinea present in the empirical chart of Dietrich [6]. This region in our M_2 model is instead dominated by an amphidromic system. The full 360° counter clockwise phase change about New Zealand is in agreement with the empirical charts.

The K_1 tidal solution in Figure 7 was compared with that of Zahel [26]. The amphidromic systems of the Atlantic and Indian Oceans correspond quite closely between the two solutions, with the exception that the zero cotidal contour runs directly between the North Atlantic and Central Atlantic amphidromes of our model rather than to the coasts of Spain and Dakar, respectively. As with the M_2 tide, the Pacific basin offers the most contrast between the numerical models.

Where Zahel finds a single dominate amphidrome in the Central Pacific, we find this region divided into two centers along an arc running from Wake Island to Tahiti. In addition we find an amphidromic system off the coast of Chile. The two models compare closely in the northeast Pacific and the South Pacific. As with the M_2 wave, general agreement is found with the K_1 empirical chart of Dietrich with the exception of the western and southeastern Pacific basin. In particular, the region of constant phase in the western Pacific found by Dietrich is dominated by an amphidromic system in our model.

Tables IV-V compare tidal amplitudes and phases of the M_2 , S_2 , K_1 , O_1 models at selected locations with the harmonic constants available from the Admiralty Tide Tables [1]. The phases are relative to the Greenwich meridian, and are the $S(\phi, \gamma)$ phases defined by Equation (33).

Figure 3

$2^\circ \times 2^\circ M_2$ (Neglecting Loading and Self-Gravitation Effects)

S: Dashed lines --- cotidal lines (phase) in hours

A: Solid lines — corange lines (amplitude) in decimeters

$$\xi(\phi, \lambda; t) = A(\phi, \lambda) \cos [\sigma t - S]$$

$$\sigma = .00014052 \text{ radians/sec}$$

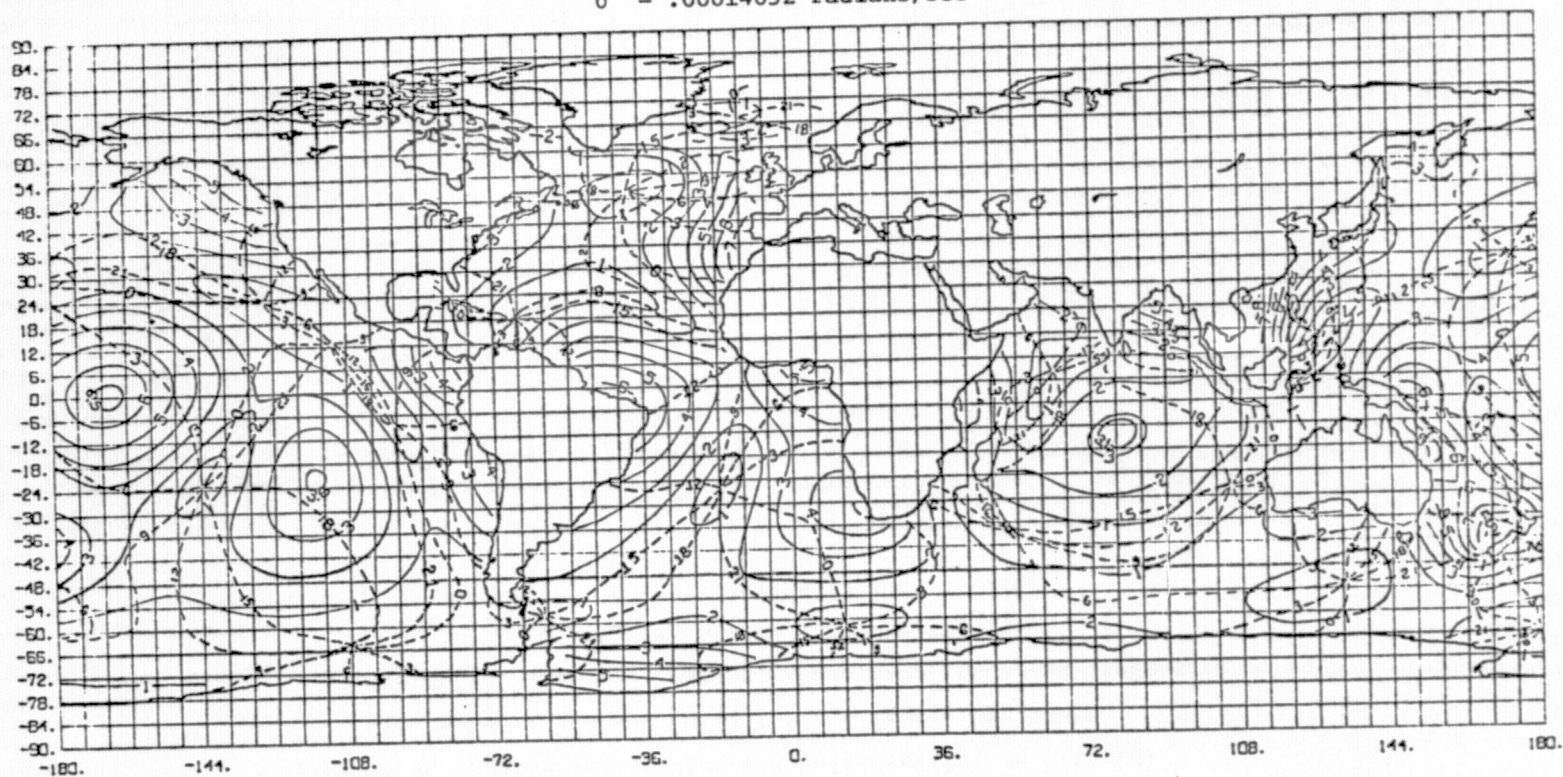


Figure 4

$2^\circ \times 2^\circ S_2$ (Neglecting Loading and Self-Gravitation Effects)

S: Dashed lines --- cotidal lines (phase) in hours

A: Solid lines — corange lines (amplitude) in decimeters

$$\xi(\phi, \lambda; t) = A(\phi, \lambda) \cos[\sigma t - S]$$

$$\sigma = .0001454452 \text{ radians/sec}$$

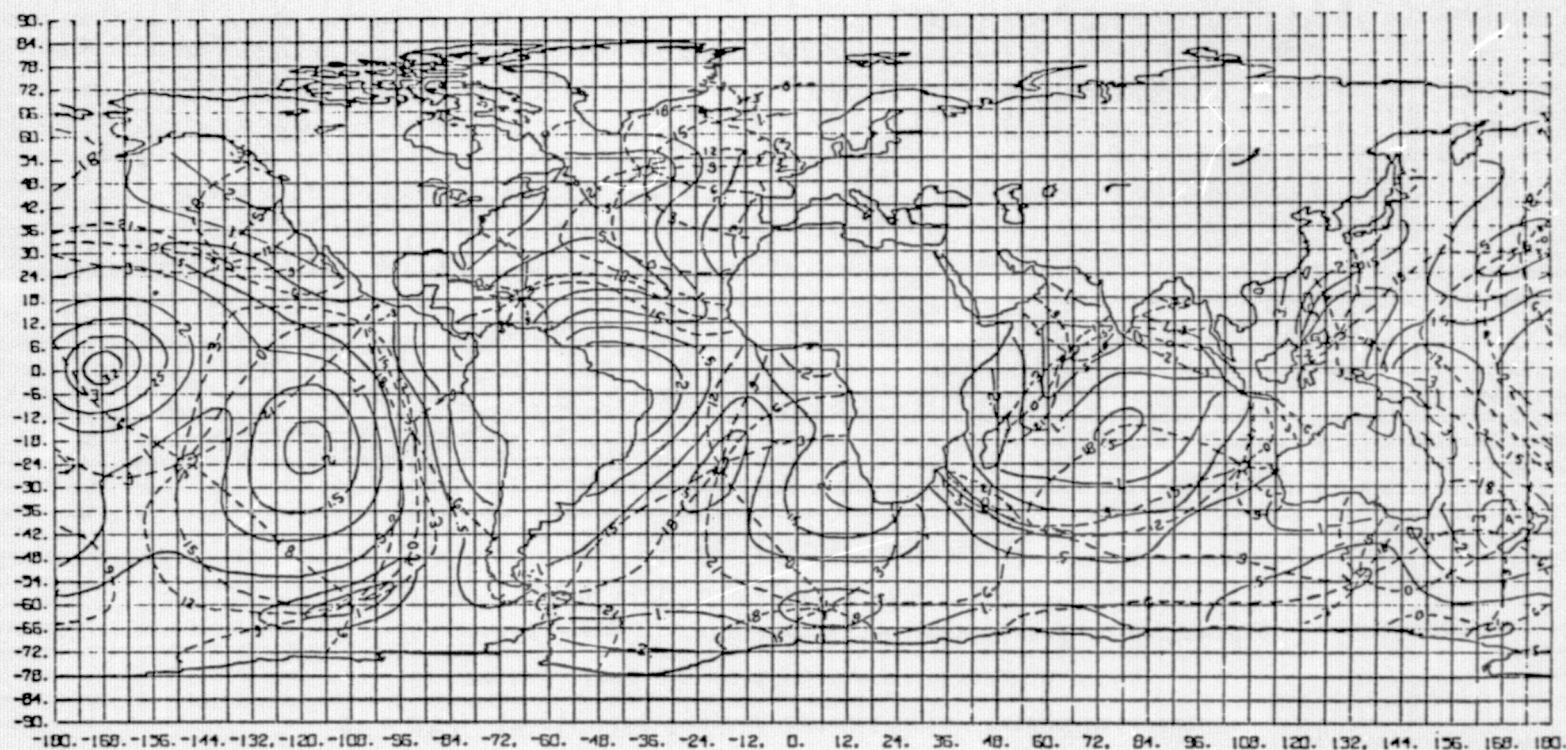


Figure 5

$2^\circ \times 2^\circ N_2$ (Neglecting Loading and Self-Gravitation Effects)

S: Dashed lines --- cotidal lines (phase) in hours

A: Solid lines — corange lines (amplitude) in centimeters

$$\xi(\phi, \lambda; t) = A(\phi, \lambda) \cos [\sigma t - S]$$

$$\sigma = .00013788 \text{ radians/sec}$$

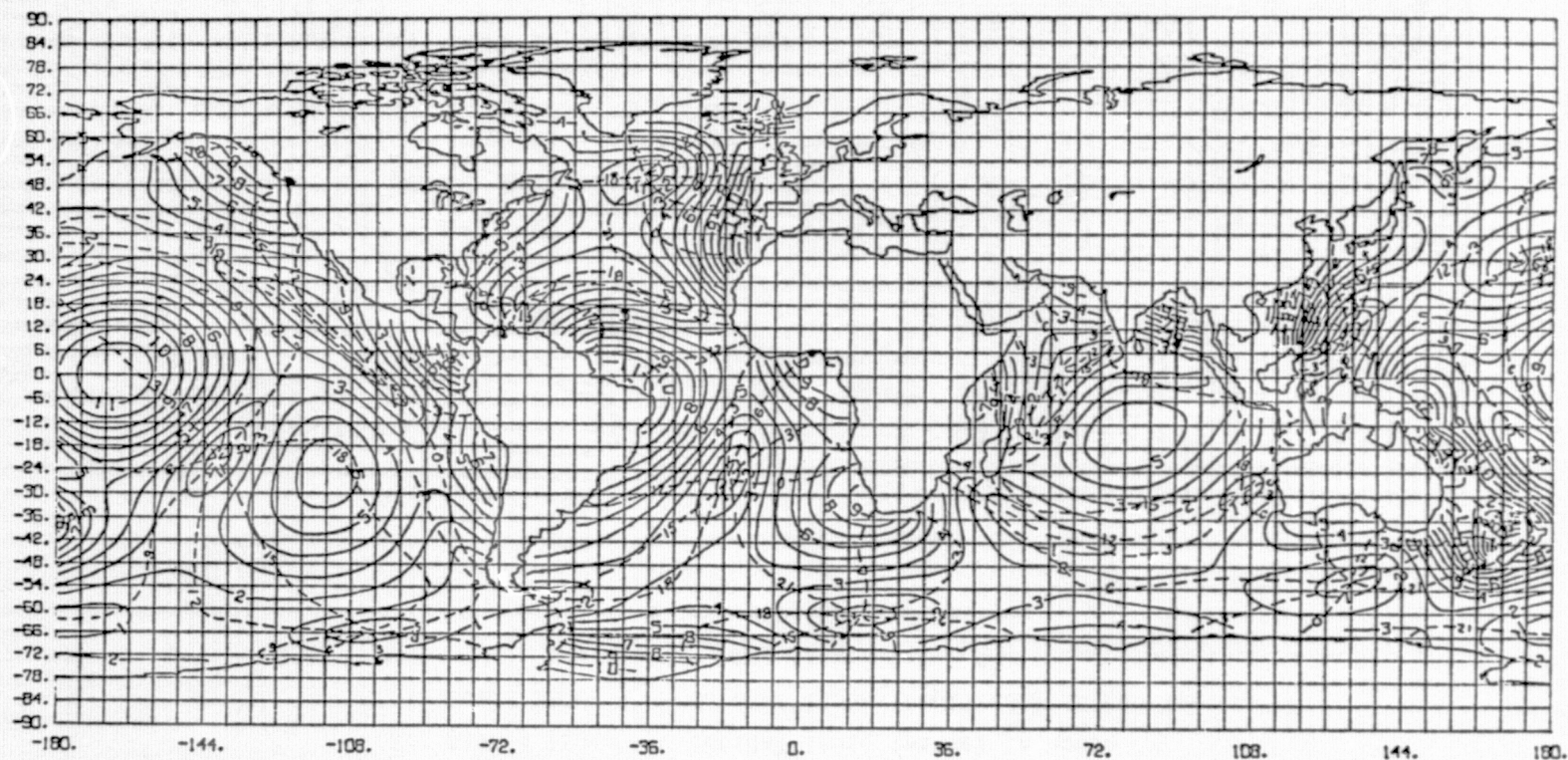


Figure 6

$2^\circ \times 2^\circ K_2$ (Neglecting Loading and Self-Gravitation Effects)

S: Dashed lines --- cotidal lines (phase) in hours

A: Solid lines — corange lines (amplitude) in centimeters

$$\xi(\phi, \lambda; t) = A(\phi, \lambda) \cos [\sigma t - S]$$

$$\sigma = .00014584 \text{ radians/sec}$$

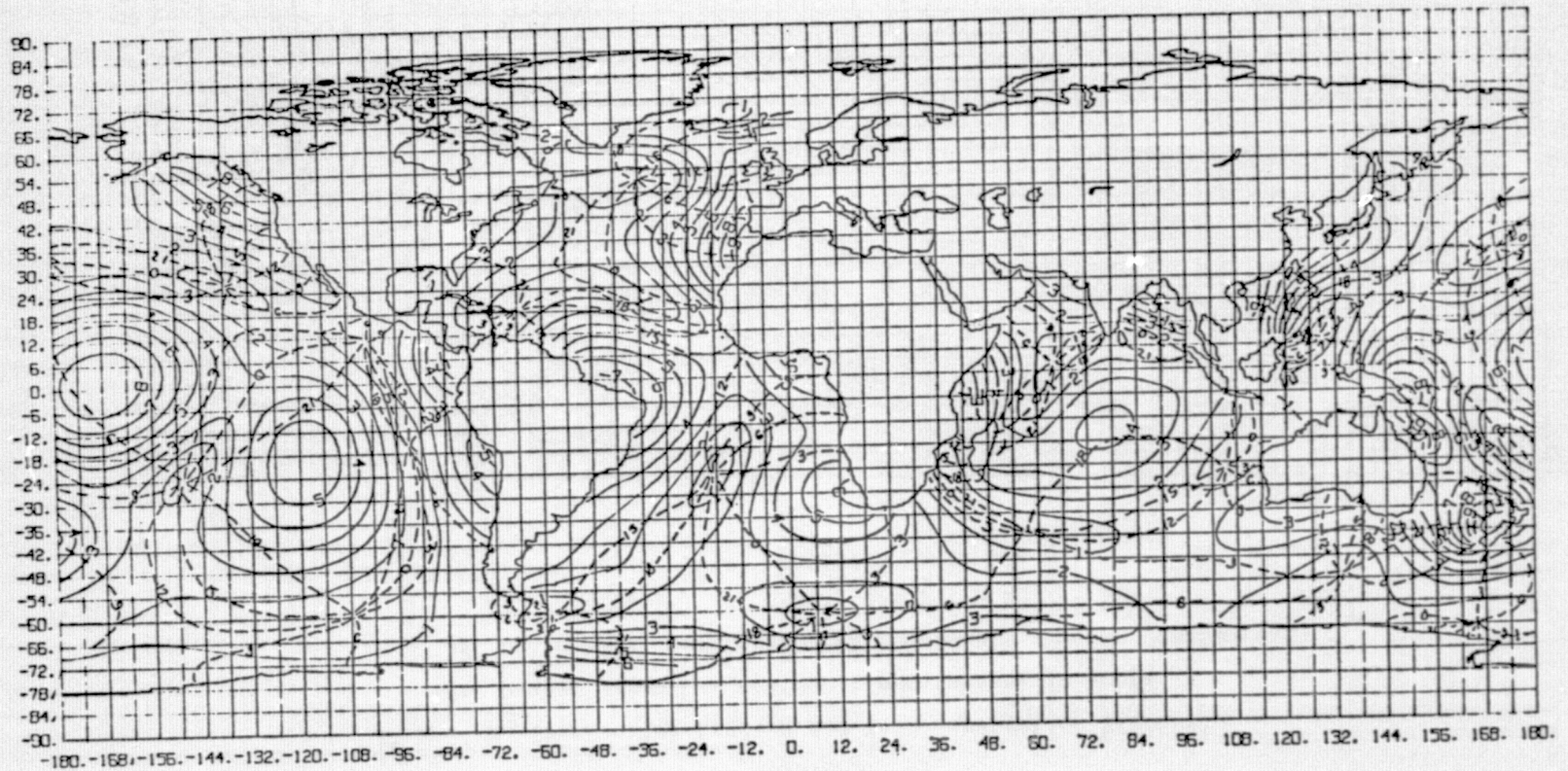


Figure 7

$2^\circ \times 2^\circ K_1$ (Neglecting Self-Gravitation and Ocean Loading Effects)

S: Dashed lines --- cotidal lines (phase) in hours

A: Solid lines — corange lines (amplitude) in decimeters

$$\xi(\phi, \lambda; t) = A(\phi, \lambda) \cos [\sigma t - S]$$

$$\sigma = .0000729216 \text{ radians/sec}$$

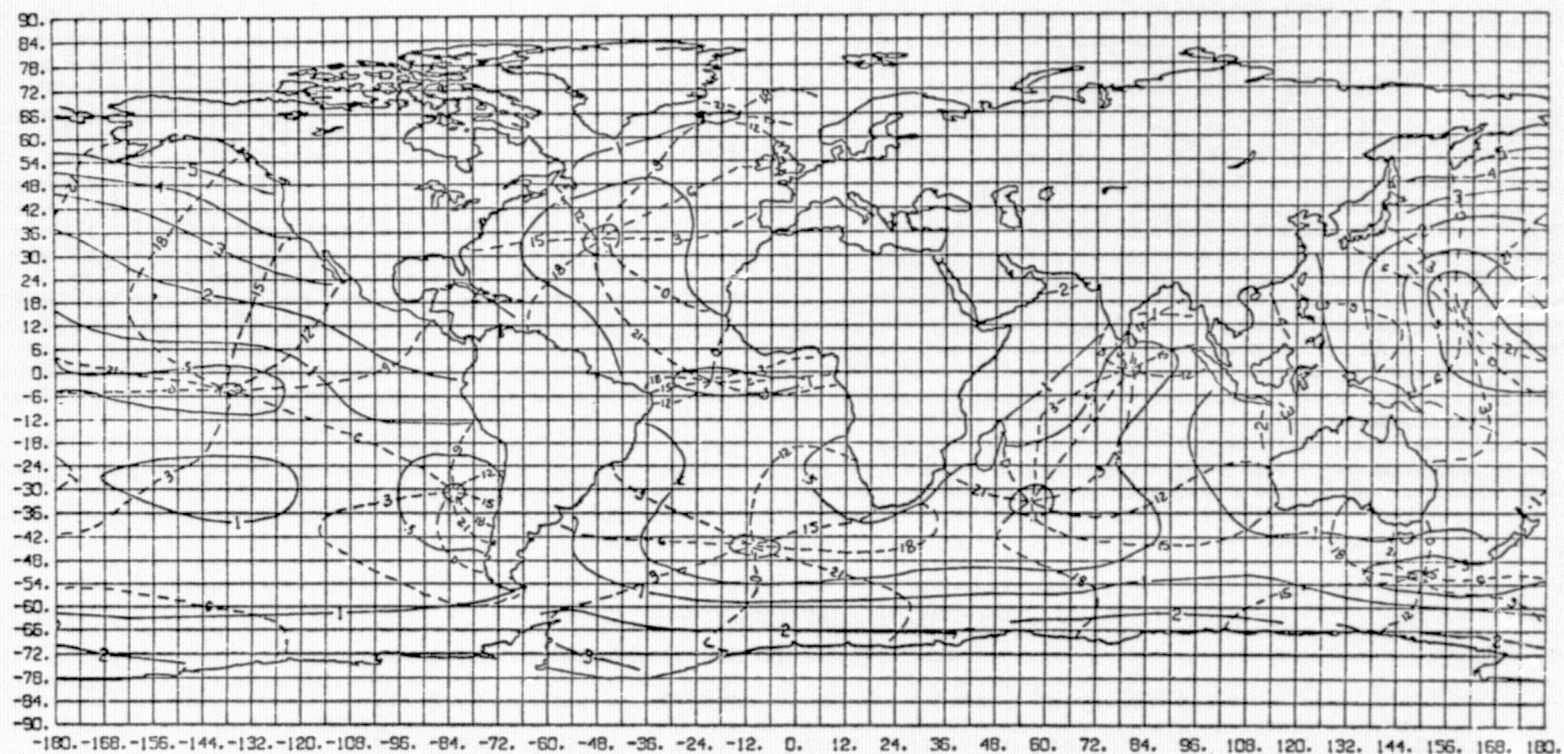


Figure 8

$2^\circ \times 2^\circ 0_1$ (Neglecting Self-Gravitation and Ocean Loading Effects)

S: Dashed lines --- cotidal lines (phase) in hours

A: Solid lines — corange lines (amplitude) in decimeters

$$\xi(\phi, \lambda; t) = A(\phi, \lambda) \cos [\sigma t - S]$$

$$\sigma = .0000675983 \text{ radians/sec}$$

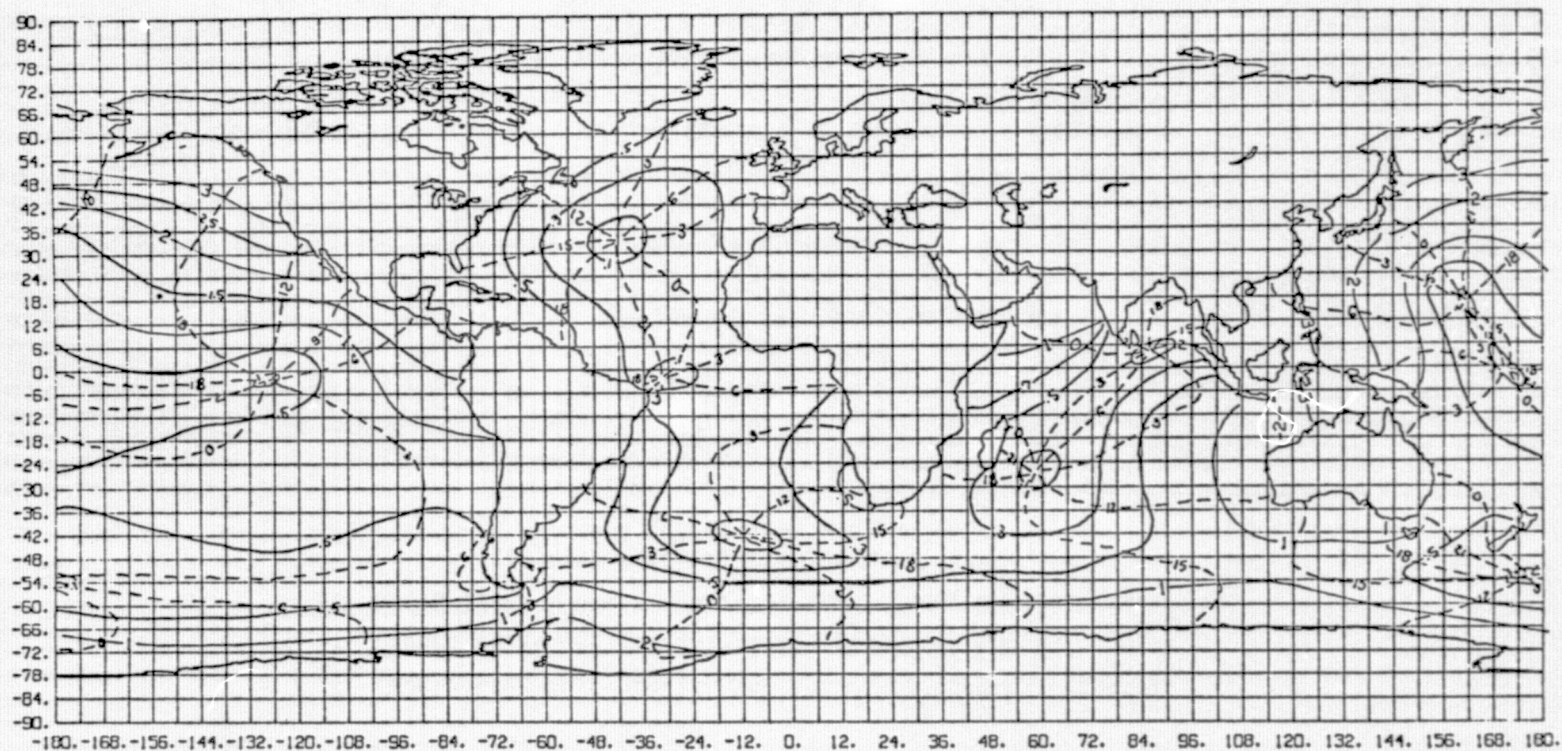


Figure 9

$2^\circ \times 2^\circ P_1$ (Neglecting Self-Gravitation and Ocean Loading Effects)

S: Dashed lines --- cotidal lines (phase) in hours

A: Solid lines — corange lines (amplitude) in decimeters

$$\xi(\phi, \lambda; t) = A(\phi, \lambda) \cos [\sigma t - S]$$

$$\sigma = .0000725236 \text{ radians/sec}$$

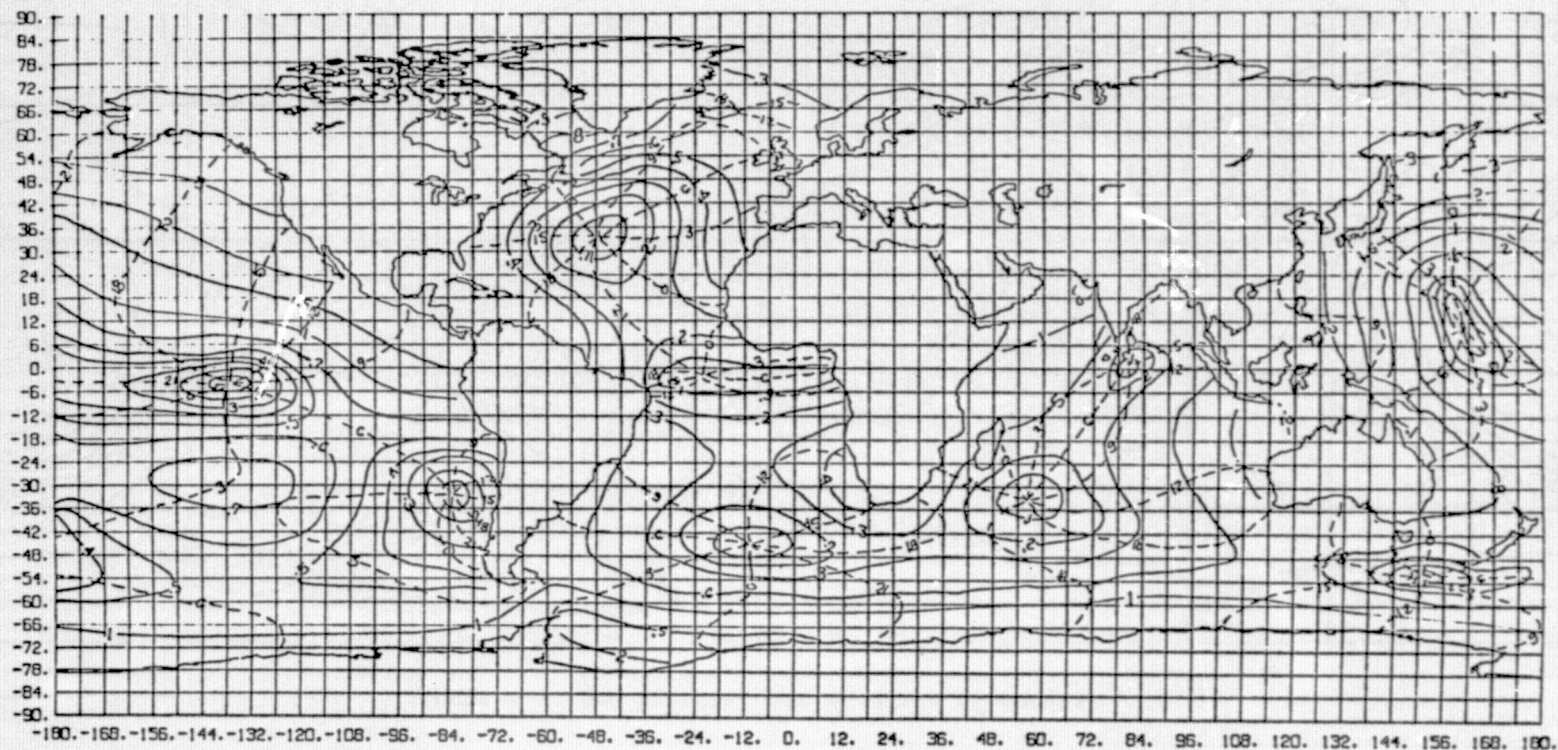


Figure 10

GLOBAL OCEAN DEPTH PROFILE

Contour Values Expressed in Hundreds of Meters

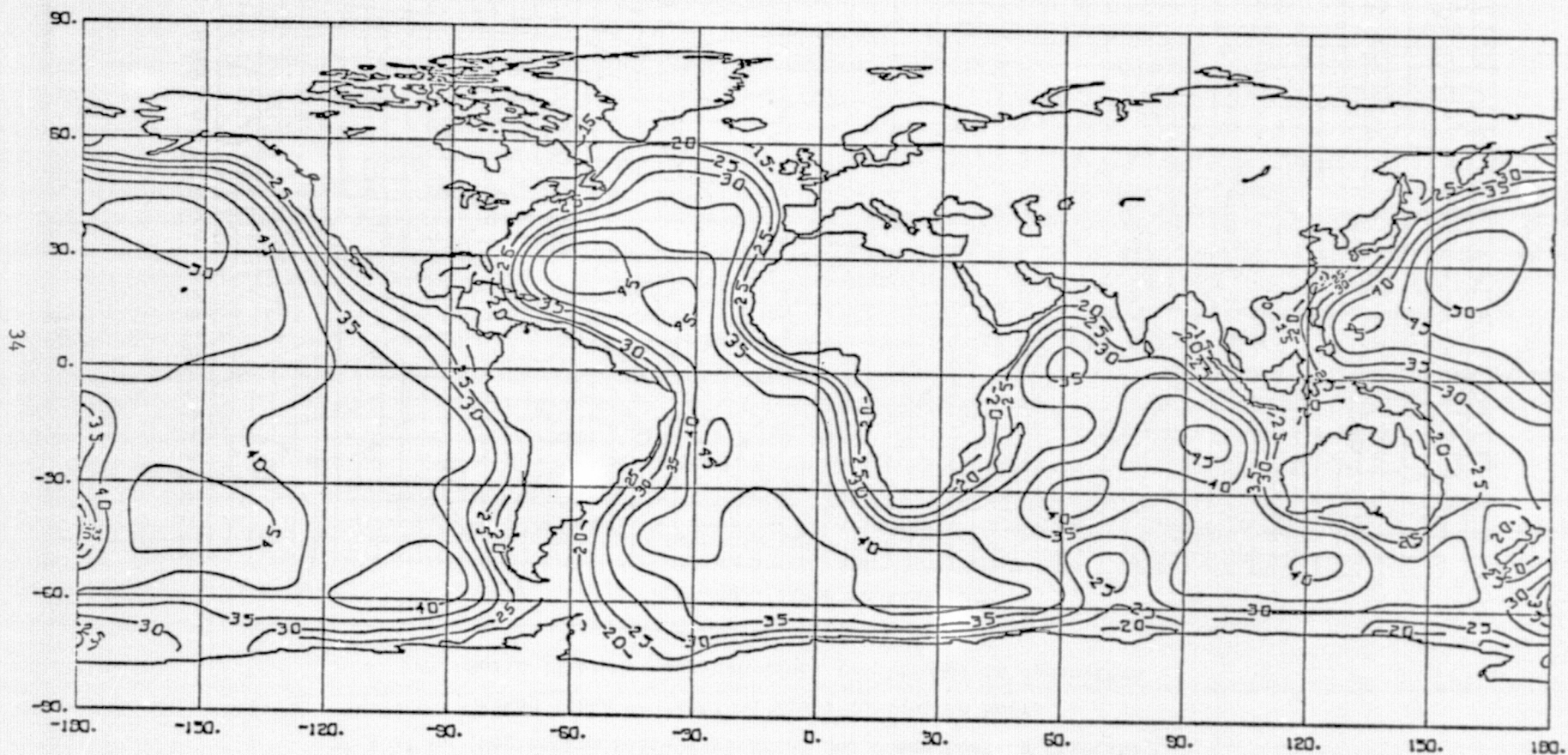


Figure 11

TIME VARIATION OF M_2 TIDAL SOLUTION IN THE CENTRAL NORTH ATLANTIC

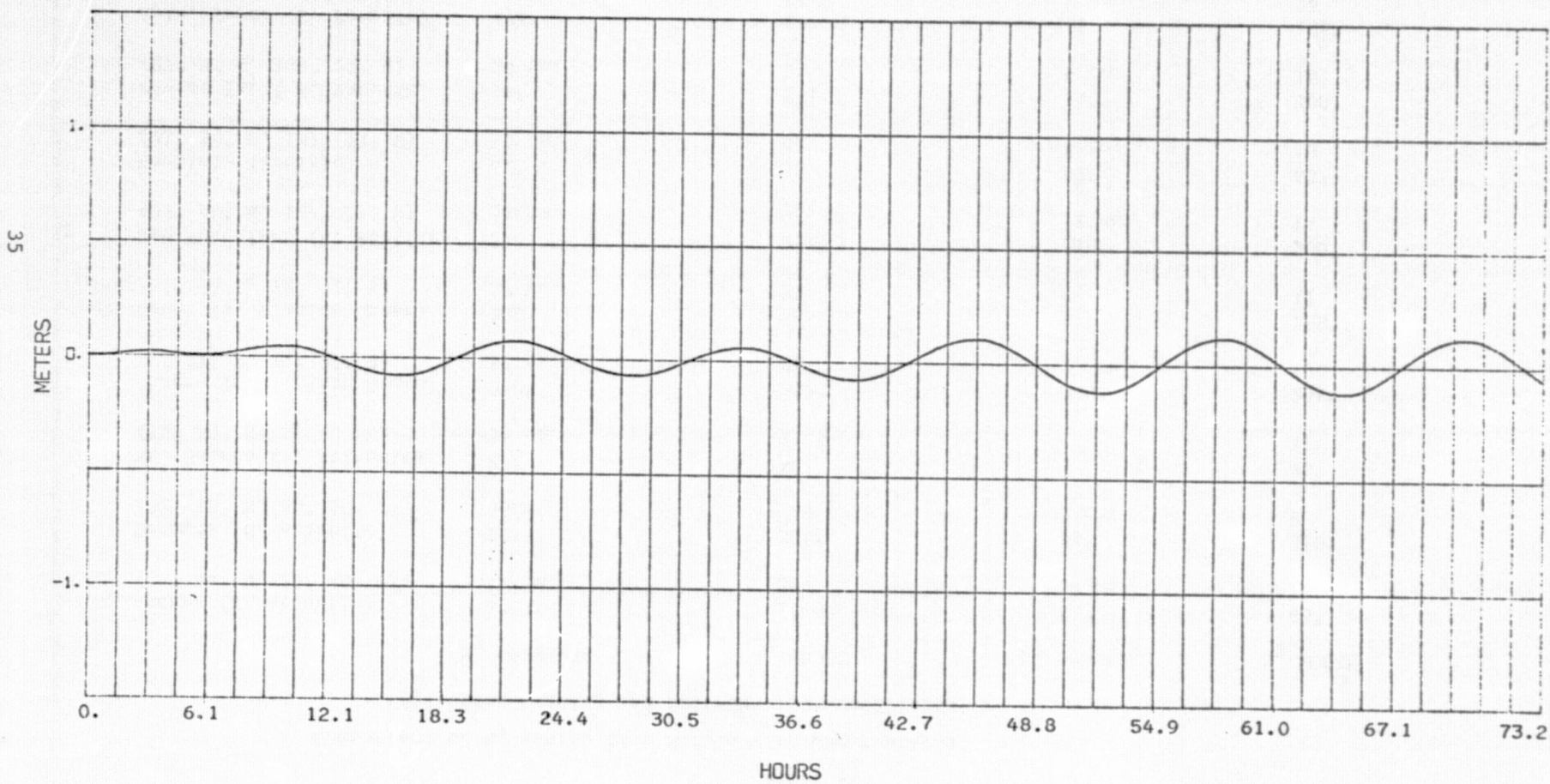


TABLE IV

Comparison of M_2 and S_2 Tide Models with Observations
(Neglecting Loading and Self-Gravitation Effects)

	M_2 OBSERVED	M_2 MODEL	S_2 OBSERVED	S_2 MODEL
Azores (N. Atlantic) (37° 44' N. 25° 40' W)	63.3° 49 cm.	26.3° 39	82°.5 18 cm.	48° 18
Bermuda (N. Atlantic) (32° 19' N. 64° 50' W)	20° 38cm.	300° 19	45° 8 cm.	310° 8
St. Helena (S. Atlantic) (15° 55' S. 5° 42' W)	87° 34 cm.	54° 25.5	-	70° 11
Chagos Is. (Indian Ocean) (7° 21' S. 72° 27' E)	270° 52 cm.	252° 26	300° 27 cm.	268° 13
Cocos Is. (Indian Ocean) (12° 5' S. 96° 51' E)	306° 27 cm.	266° 22	5° 9 cm.	288° 12
San Francisco (E. Pacific) (37° 48' N. 122° 27' W)	215° 54 cm.	195° 35 cm.	210° 12 cm.	200° 14
Honolulu (Pacific) (21° 18' N. 157° 52' W)	61° 16 cm.	35 33	62° 5 cm.	63° 13
Easter Is. (S. Pacific) (27° 9' S. 109° 27' W)	32° 20 cm.	281° 35	240° 6 cm.	300° 16
Apia, Samoa (S. Pacific) (13° 48' S. 171° 46' W)	171° 38 cm.	87° 54	150° 9 cm.	105° 24
Siapan (S. Pacific) (15° 12' N. 145° 43' E)	300° 17 cm.	159° 21	315° 5 cm.	190° 9
Yaruto, Marshall Is. (S. Pacific) (5° 55' N. 169° 39' E)	125° 47 cm.	88° 46	150° 26 cm.	109° 23
Burgana, Solomon Is. (S. Pacific) (9° 11' S. 160° 13' E)	134° 11 cm.	196° 33	180° 8 cm.	210° 15

TABLE V

Comparison of K_1 and O_1 Tide Models with Observations
(Neglecting Loading and Self-Gravitation Effects)

	K_1 OBSERVED	K_1 MODEL	O_1 OBSERVED	O_1 MODEL
Azores (N. Atlantic) (37° 44' N. 25° 40' W)	66° 4 cm.	70° 4.6	315° 3 cm.	80° 2
Bermuda (N. Atlantic) (32° 19' N. 64° 50' W)	195 7 cm.	230° 4	210° 5 cm.	220° 3.5
St. Helena (S. Atlantic) (15° 55' S. 5° 42' W)	-	165° 3	-	137° 2
Chagos Is. (Indian Ocean) (7° 21' S. 72° 27' E)	84° 3 cm.	80° 4	60° 3 cm.	62° 3
Cocos Is. (Indian Ocean) (12° 5' S. 96° 51' E)	165° 11 cm.	168° 11	127° 9 cm.	139° 8.5
37 San Francisco (E. Pacific) (37° 48' N. 122° 27' W)	228° 37 cm.	229° 43	210° 23 cm.	193° 29
Honolulu (Pacific) (21° 18' N. 157° 52' W)	225° 15 cm.	266° 19	225° 8 cm.	230° 15
Easter Is. (S. Pacific) (27° 9' S. 109° 27' W)	18° 8 cm.	57° 8	9° 5 cm.	17.5° 8
Apia, Samoa (S. Pacific) (13° 48' S. 171° 46' W)	75° 5 cm.	28° 7	60° 3 cm.	340° 3
Siapan (S. Pacific) (15° 12' N. 145° 43' E)	75° 14 cm.	130° 11	45° 10 cm.	82° 11
Yaruto, Marshall Is. (S. Pacific) (5° 55' N. 169° 39' E)	75° 9 cm.	306° 3	45° 6 cm.	2
Burgana, Solomon Is. (S. Pacific) (9° 11' S. 160° 13' E)	45° 20 cm.	60° 8	22° 11 cm.	57° 6

4.7 M₂ Tide Including Ocean Loading and Self-Gravitation

The solutions of Section 4.6 show general agreement with empirical solutions with respect to the positions of amphidromic systems and tidal amplitudes. Notable exceptions to the agreement of the theoretical with empirical solutions are in the western and southeastern portions of the Pacific basin. Phase relations also differ in portions of the North and South Atlantic. To improve the M₂ model of Section 4.6, the method of successive approximations outlined in Section 2.0 was used to solve the IDLTE given by Equation (14) on a 3° x 3° global grid. The M₂ solution of Section 4.6 was used as the initial solution.

The convergence of the procedure was slow in the southeastern Pacific basin, requiring 16 iterations to reach final convergence. Convergence in all other regions was more rapid, requiring approximately 8 iterations. (convergence was considered to be achieved when the corange and cotidal lines no longer changed from one iteration to another). To assure that the iteration procedure had stabilized, two additional iterations (18 iterations) were calculated. Figure 12 displays the self-gravitation and ocean loading potential Γ' obtained by evaluating Equations (15) with the initial solution from Section 4.6 (the 0th order approximation). The portions of Γ' due to self-gravitation only and crustal deformation only (U' Green's Function) are displayed in Figures 13 and 14 respectively. The converged M₂ solution (16th iteration) is presented in Figure 15.

Comparison shows no large differences in amplitude or position of amphidromes between the M₂ solution of Section 4.6 and that of Figure 15 which includes the perturbing effects of ocean self-gravitation and crustal loading. There are, however, significant changes in phase. In particular, the phases of the North Atlantic amphidrome are rotated clockwise approximately 25° and the phases from the South Atlantic amphidrome are rotated clockwise by 45° along the South American coast and approximately 20° along the equatorial coast of Africa. These shifts in phase improve agreement with observations in the Atlantic as demonstrated by the comparisons at Bermuda, the Azores and St. Helena in Table VI. The rotation of phases by approximately 20° in a counter clockwise manner about the amphidrome off the west coast of Australia likewise improves agreement with observations in the Indian Ocean, as demonstrated by

Figure 12

$3^\circ \times 3^\circ M_2$ Potential $\frac{\Gamma'}{g}$ (ON ZEROth ITERATION)

S: Dashed lines --- cotidal lines (phase) in hours

A: Solid lines — corange lines (amplitude) in centimeters

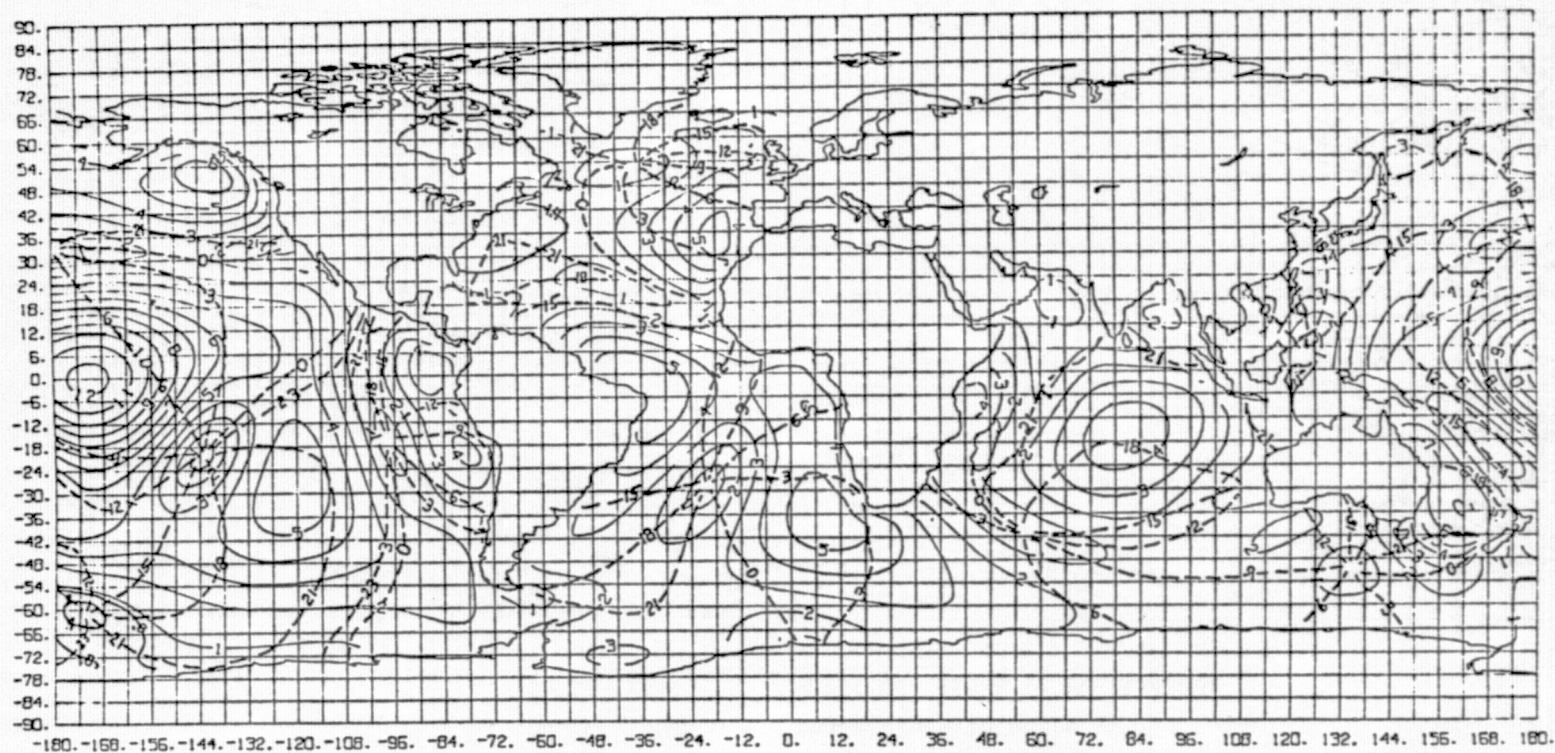


Figure 13

$3^\circ \times 3^\circ M_2$ Self-Gravitation Potential only $\frac{\Gamma'}{g}$ (ON ZEROth ITERATION)

S: Dashed lines - - - phase lines in hours

A: Solid lines _____ amplitude lines in centimeters

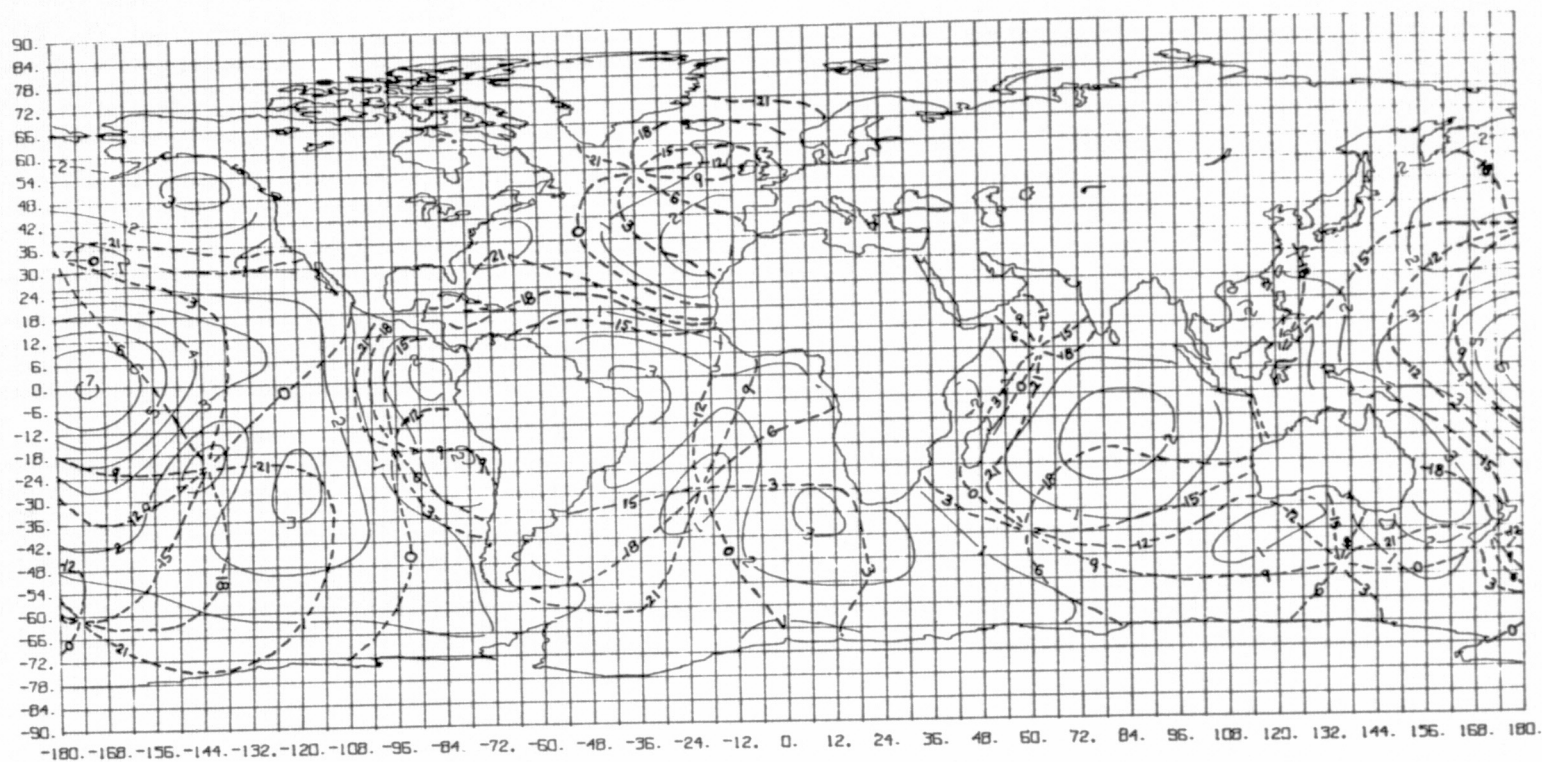


Figure 14

$3^\circ \times 3^\circ$ Crustal Response to M_2 Ocean Tidal Loading (ON ZEROth ITERATION)

S: Dashed lines --- phase lines in hours

A: Solid lines — amplitude lines in centimeters

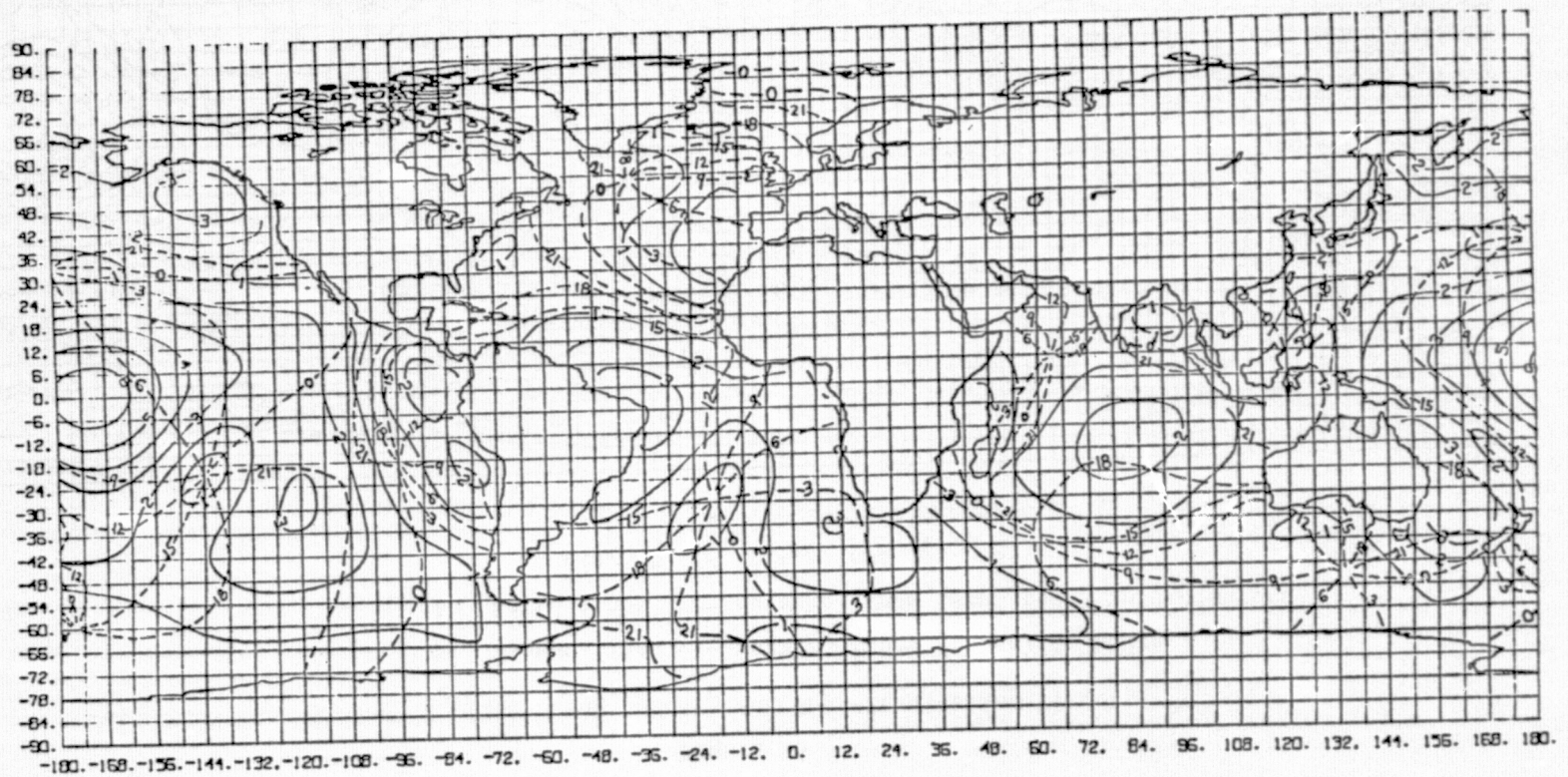


Figure 15

$3^\circ \times 3^\circ M_2$ (Including Loading and Self-Gravitation Effects)

S: Dashed lines --- cotidal lines (phase) in hours

A: Solid lines — corange lines (amplitude) in decimeters

$$\xi(\phi, \lambda; t) = A(\phi, \lambda) \cos [\sigma t - S]$$

$$\sigma = .00014052 \text{ radians/sec}$$

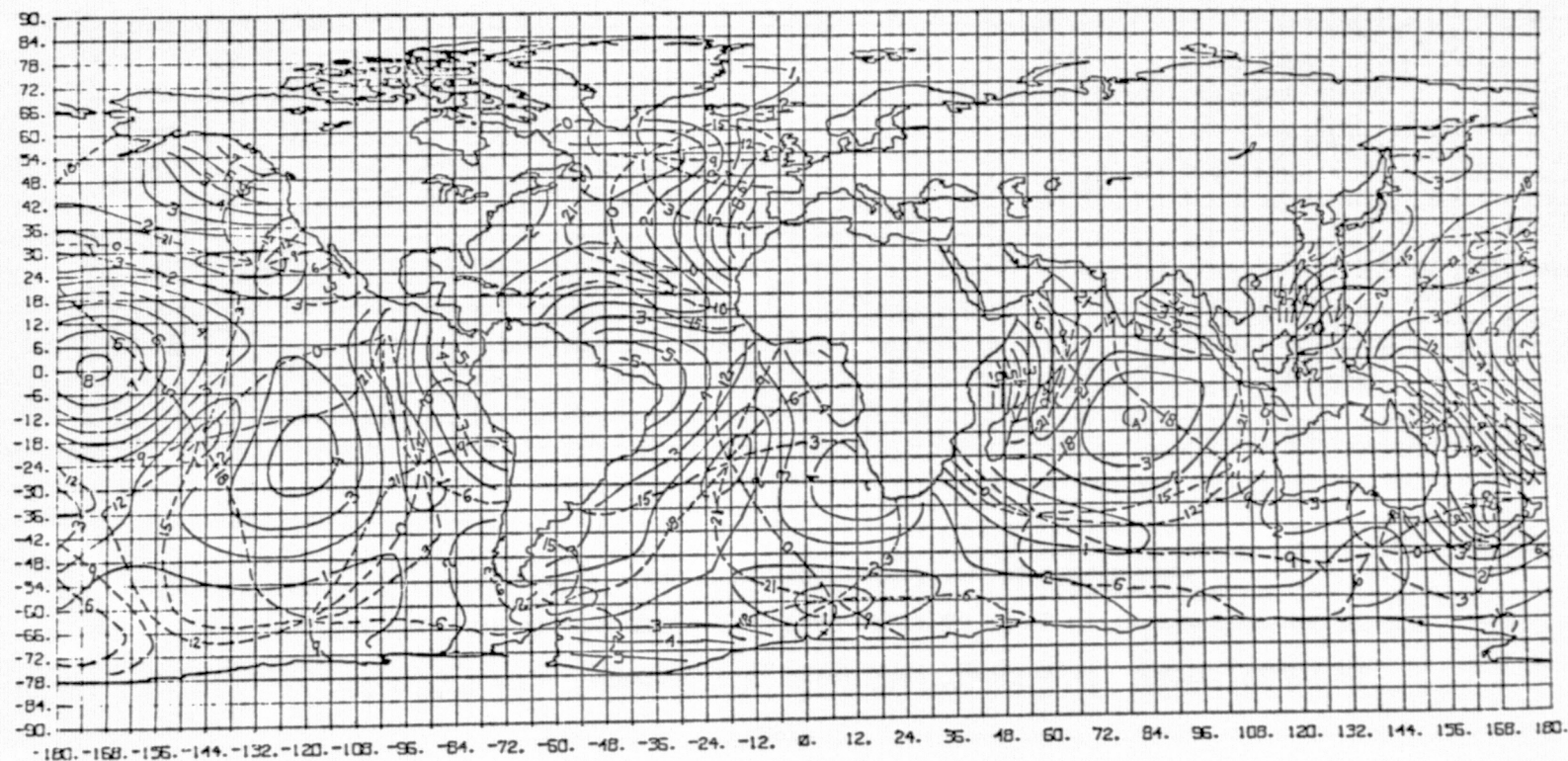


TABLE VI

M₂ OCEAN TIDE PHASE AND AMPLITUDE

	<u>OBSERVED</u>	<u>THEORETICAL</u> (Without Ocean Loading and Self-Gravitation)	<u>THEORETICAL</u> (With Ocean Loading and Self-Gravitation)
Azores (N. Atlantic) (37° 44' N. 25° 40' W)	63.3° 49 cm.	26.3° 39	50° 41
Bermuda (N. Atlantic) (32° 19' N. 64° 50' W)	20° 38 cm.	300° 19	308° 17
St. Helena (S. Atlantic) (15° 55' S. 5° 42' W)	87° 34 cm.	54° 25.5	73° 26.2
Chagos Is. (Indian Ocean) (7° 21' S. 72° 27' E)	270° 52 cm.	252° 26	269° 31
Cocos Is. (Indian Ocean) (12° 5' S. 96° 51' E)	306° 27 cm.	266° 22	285° 29
San Francisco (E. Pacific) (37° 48' N. 122° 27' W)	215° 54 cm.	195° 35 cm.	210° 45 cm.
Honolulu (Pacific) (21° 18' N. 157° 52' W)	61° 16 cm.	35 33	66° 31
Easter Is. (S. Pacific) (27° 9' S. 109° 27' W)	32° 20 cm.	281° 35	303° 34
Apia, Samoa (S. Pacific) (13° 48' S. 171° 46' W)	171° 38 cm.	87° 54	112° 55
Siapan (S. Pacific) (15° 12' N. 145° 43' E)	300° 17 cm.	159° 21	200° 25
Yaruto, Marshall Is. (S. Pacific) (5° 55' N. 169° 39' E)	125° 47 cm.	88° 46	114° 53
Burgana, Solomon Is. (S. Pacific) (9° 11' S. 160° 13' E)	134° 11 cm.	196° 33	210° 34

comparisons at Chagos Island and Cocos Island. In the Pacific northeast, the phase lines radiating from the amphidrome off the California coast are rotated clockwise by approximately 15° improving the model along the North American western seaboard. The only appreciable shift of an amphidrome involves the system off the coast of Ecuador, which moves southward by approximately 15° of latitude as well as being rotated clockwise by 45° . The amphidrome which dominates the northwest Pacific basin experiences a 45° counter clockwise shift of the phase lines along the Asian coast making phases along Japan and Okinawa more realistic. Agreement of the M_2 solution including ocean loading and self-gravitation effects with island observations is generally within 30° of phase and 25 cm. is amplitude. Exceptions are along the Aleutians, in the Sargasso Sea region and the southeastern Pacific basin. (see Table VI).

Solutions for K_1 and S_2 including the effects of ocean loading and self-gravitation are currently being calculated and will be presented in a later publication.

4.8 Total Tide Comparison with Observations

The complexity of the total tide becomes evident when the seven constituent models are combined to yield an approximation to the total ocean tide. The theoretical global ocean tide models are not expected to be realistic along highly irregular coast lines or in shallow water along continental coasts due to the assumptions imposed in the boundary conditions. Deep ocean islands, such as the principal ports of Honolulu, Bermuda and the Azores of the Admiralty Tide Tables provide a reasonable means of comparing the ocean tide models with observations. It must be remarked, however, that groups of islands, too small to be included in the global model, can strongly influence the tides in their vicinity. Figures 16 - 19 display the tide composed of the S_2 , N_2 , K_2 , K_1 , O_1 , P_1 models of Section 4.6 and the M_2 model of Section 4.7 for the Azores, Bermuda, San Francisco and Honolulu. Times and values of high and low water from the Admiralty Tide Tables are indicated on the plots. The comparison at the Azores, which is dominated by the M_2 Tide, is very good, while the predicted tide at Bermuda displays a reasonable phase but small amplitude (see also Table VI). The tides at San Francisco and Honolulu show a greater diurnal influence. The phases and amplitudes of the predicted tide at San Francisco are reasonable, while the predicted tide at Honolulu shows poorer agreement. Causes for possible disagreement between observations and the theoretical models were discussed in Section 1.0.

Figure 16

Tide Model Prediction for Azores, Jan. 1, 2 1977
(Circled Points are Observed High and Low Waters)

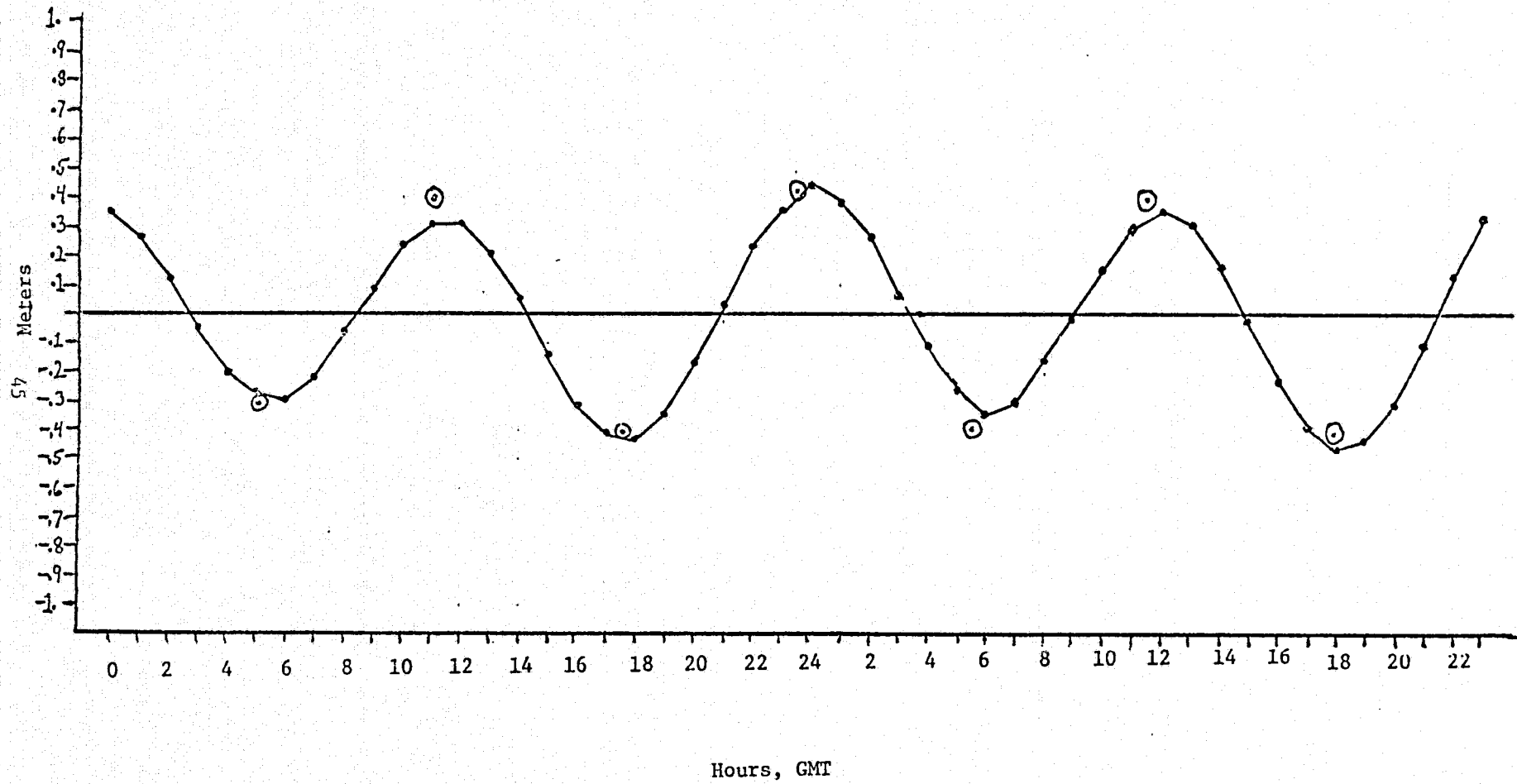


Figure 17

Tide Model Prediction for Bermuda, Jan. 1, 2 1977
(Circled Points are Observed High and Low Waters)

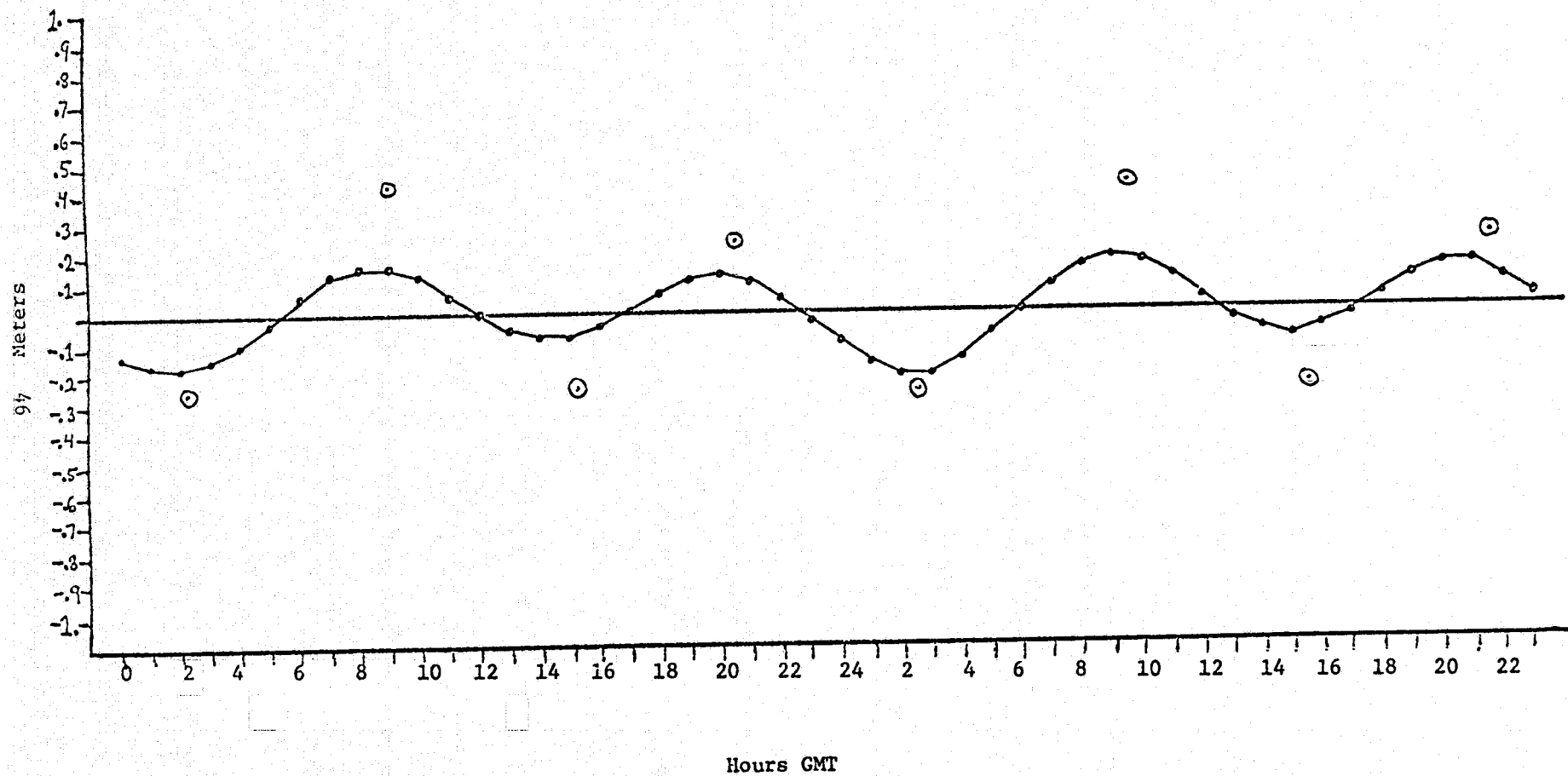


Figure 18
Tide Model Prediction for San Francisco, Jan. 1, 2 1977
(Circled Points are Observed High and Low Waters)

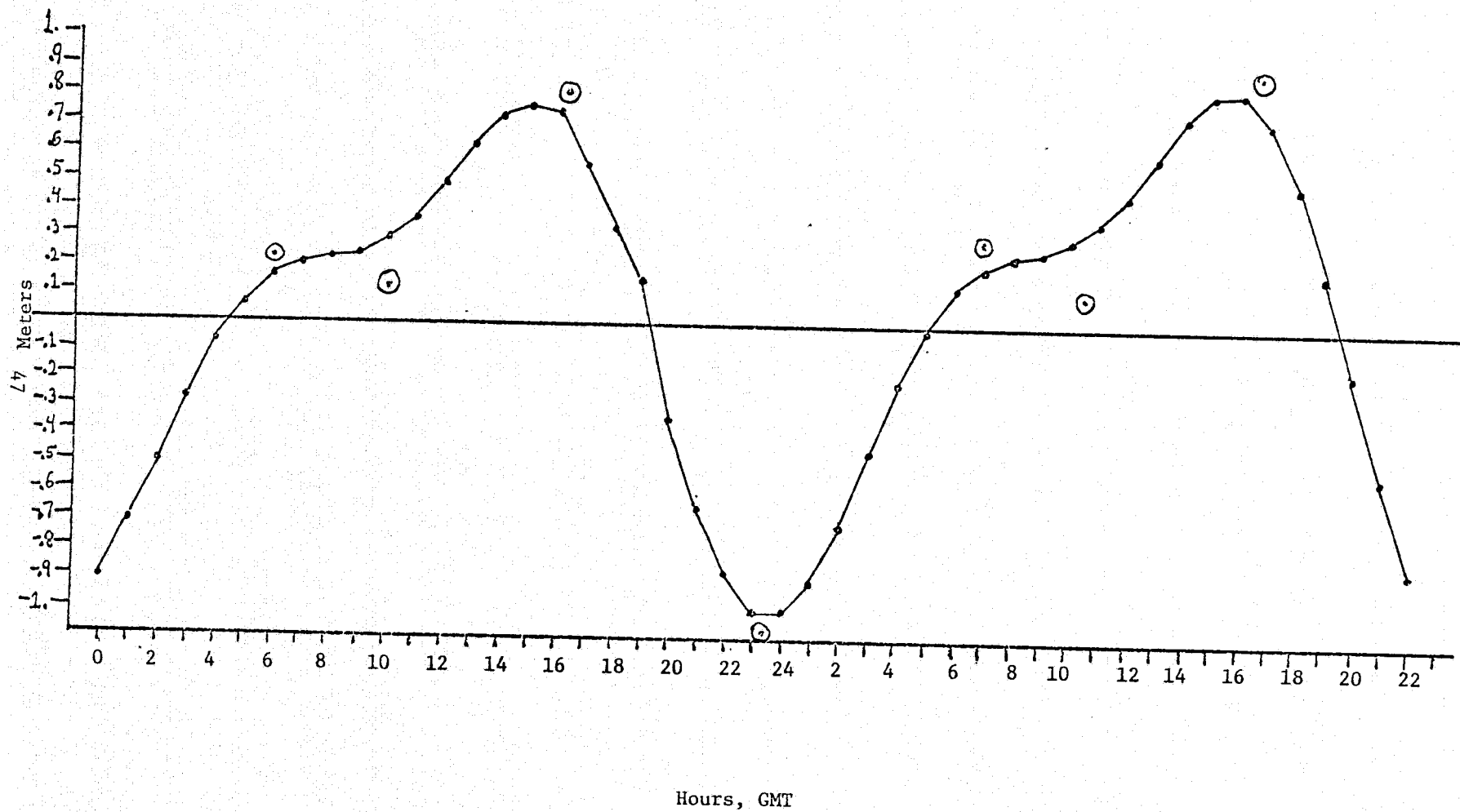
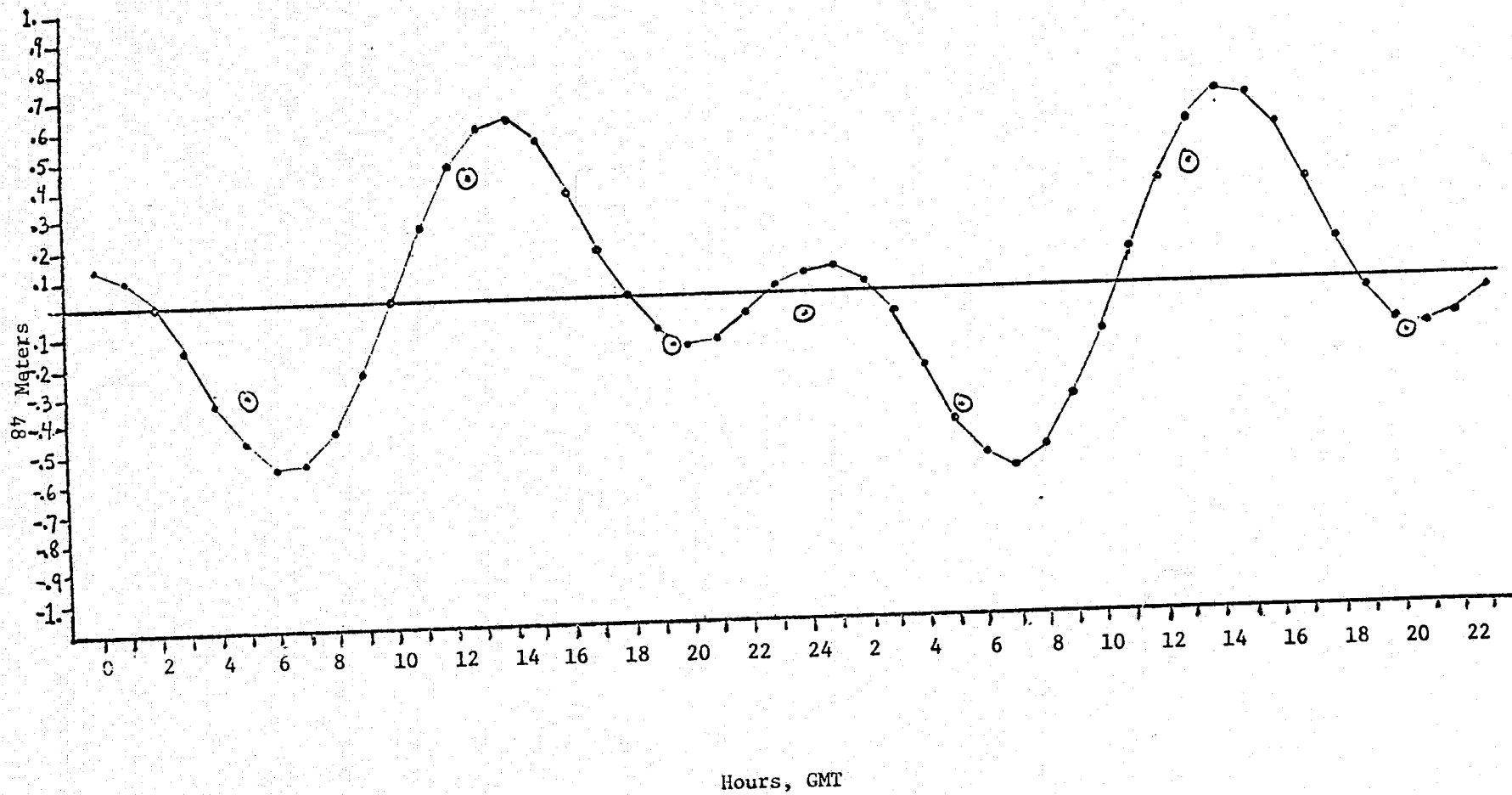


Figure 19
Tide Model Prediction for Honolulu, Jan. 1, 2 1969
(Circled Points are Observed High and Low Waters)



5.0 Computer Software System

The integro-differential IDLTE Software System is composed of three basic modules:

- I. IDLTE Integration Package. This program integrates the system described by Equation (14) of Section 2.0. It requires as input the prescribed continental boundaries, the global ocean depth profile defined on a grid, an initial solution, and the potential Γ' . To calculate the zeroth order solution both the initial solution and Γ' are set to zero.
- II. Surface Integration Package. This program evaluates the potential Γ' of Equation (15) of Section 2.0. It requires as input the prescribed continental boundaries, a specified global tide $\xi(\phi, \lambda)$ in the form of gridded amplitude and phase values and a table of values for the Green's functions ϕ' and U' of Equation (5) as a function of angle.
- III. Ocean Loading Green's Function Package. This program evaluates a table of the Green's functions ϕ' and U' of Equation (35) from an input set of load Love numbers k'_n and h'_n .

The three modules are written in FORTRAN IV, and Modules I and II are designed with a modified graphics package (WOLF PLOT PACKAGE) for solution display. The I/O design of the system uses multiple magnetic tape drives. Table VIII defines the I/O units for Modules I and II.

5.1 Program Input

User control of Modules I and II is set up by card input for the principal variables through a NAMELIST specification. The variable names, their function and their default values are presented in Tables IX and X. The ocean depth values required for Module I are read from an external tape, with values defined on a world grid (depth values on ocean grid points and 0 on land grid points).

Following the NAMELIST INPUT for both Modules I and II, the continental boundary data is input. The ocean boundaries are instituted as horizontal and vertical segments on the grid with horizontal boundaries along v velocity

points and vertical boundaries along u velocity points. The coastal boundary configuration is input by cards in a special compact format. For each latitude on the world integration grid there is a data card of the format 14I5 with fields.

LAT NO IDATA(12)

where LAT is the latitude in degrees, NO is an integer 0 or 1 depending on whether the point at zero longitude at the particular latitude is on land or ocean, respectively, and the array IDATA is the value of the longitude, in degrees, at each grid point for that latitude where a land-water boundary occurs. With this input technique any arbitrary coastal boundary configuration may be implemented. The boundary configuration presently employed is a realistic $1^\circ \times 1^\circ$ world ocean boundary. The user specified grid size extracts the proper ocean boundary from this $1^\circ \times 1^\circ$ base.

For Module II, the ocean boundary data is followed by a table of values for the Green's Functions $U'(\gamma)$ and $\Phi'(\gamma)$ for $\gamma=0^\circ, 1^\circ, 2^\circ, \dots, 180^\circ$ (scaled by $(R\gamma) \times 10^{-12}$ as discussed in Section 4.5). The input format is 8F10.3.

Module III is a stand-alone program designed to calculate the Green's Functions Φ' and U' as described in Section 4.5. The program need only be run when a new set of load Love number h'_n and k'_n are employed to calculate new functions Φ' and U' . The data for the program consists entirely of values of h_∞ , k_∞ and h'_n , k'_n for a set of values of n . This data is input in data statements within the main program of Module III.

Table VII
MODULE I SUBROUTINES

<u>Subroutine Name</u>	<u>Function</u>
SPLASH	The executive program which reads Namelist Input and calls the working subroutines of the system. This subroutine contains a BLOCK DATA subroutine.
MAINA	The module which reads the input coastal boundary data and sets up the world function (0 on land points and 1 on ocean points) corresponding to the selected integration grid size. Prints the world function to display boundaries and defines the transformations from the global grid to the compacted ocean arrays.
TIDPLT	The plotting module which generates corange contours, cotidal lines and time series plots for selected geographic points.
FUNS	The function subroutine which evaluates the derivatives of the tidal component for use in the driving terms of the Laplace Tidal Equations.
ALGR	The integration algorithm for the Laplace Tidal Equations.
DEPTH	The module which transforms the input ocean depths defined on a world grid to the compacted ocean grid.
SWRTR	INPUT/OUTPUT routine for the world grid ocean depth values.
ZARY	The module which transforms the compacted ocean arrays onto world grids for display and plotting purposes.

Table VIII
TAPE I/O UNITS FOR MODULES I & II

Module	I/O Unit	Function
Module I	30	INPUT - World ocean depth profile
	40	INPUT - Initial tide solution
	50	OUTPUT - Tide solution cotidal and corange values
	60	OUTPUT - Time series of tide heights over the span of integration for three specified geographic location.
	70	INPUT - $\frac{\partial P}{\partial \lambda}, \frac{\partial P}{\partial \phi}, \frac{\partial Q}{\partial \lambda}, \frac{\partial Q}{\partial \phi}$
	80	OUTPUT - Tide solution ξ at the final integration time.
<hr/>		
Module II	30	INPUT - Tide solution cotidal and corange values (from unit 50 of Module I)
	40	OUTPUT - Tide perturbation potential Γ' in cotidal and corange form.
	50	OUTPUT - $\frac{\partial P}{\partial \lambda}, \frac{\partial P}{\partial \phi}, \frac{\partial Q}{\partial \lambda}, \frac{\partial Q}{\partial \phi}$

Table IX

MODULE I NAMELIST VARIABLES

Variable Name	Function	Default Value
DDEL	Integration time step in minutes.	(6.)
TTN	Integration start time in minutes when the restart option is used.	(0.)
BR	Radius of the earth in meters.	(6371×10^3)
SR	Friction coefficient, C_r .	(.003)
AH	Coefficient of lateral turbulent viscosity, C_{hv} , in meters ² /sec.	(1×10^7)
K	Dimensionless "general lunar coefficient" $\frac{3}{2} \frac{M_{\text{moon}}}{M_{\text{earth}}} \left(\frac{R_E}{R_{\text{moon}}} \right)^3$ <p>where M denotes mass, R_E the earth's radius and R_{moon} the mean lunar distance.</p>	$(.842 \times 10^{-7})$
K2	Love number which represents the coefficient of additional potential due to deformation by a non-loading potential.	(0.)
CT	Amplitude factor for tidal constituent. (\bar{C} of Eq (25))	(1.)
SLG	Tidal constituent frequency in rad/sec.	$(.1405 \times 10^{-3})$
G	Gravitational acceleration in meters/sec ² .	(9.81)
W	Rotational rate of the earth in rad/sec.	$(.72722 \text{ E-4})$
ND	Grid size in degrees.	(6°)
IFLGR	Restart Flag	(0)
	0 - Start integration from t=0 from zero initial solution.	
	1 - Read tidal solution at time TTN from I/O Unit 40 and integrate over 1/4 tidal period; Form corange and cotidal solutions.	
	2 - Read tidal solution at time TTN from I/O Unit 40 and integrate over NITR tidal periods.	

Table IX (Cont.)
MODULE I NAMELIST VARIABLES

<u>Variable Name</u>	<u>Function</u>	<u>Default Value</u>
IPERT	Perturbation Flag	(0)
	0 - No perturbation potential Γ' included in equations of motion.	
	1 - Read $\frac{\partial P}{\partial \lambda}$, $\frac{\partial P}{\partial \phi}$, $\frac{\partial Q}{\partial \lambda}$, $\frac{\partial Q}{\partial \phi}$ from I/O Unit 70, and include Γ' potential in equations of motion.	
NOO	Lower latitude limit in degrees for global integration. NOTE: The difference between -90° and NOO must be an integer times the grid size ND.	(-78°)
NEE	Upper latitude limit in degrees for global integration. NOTE: The difference between 90° and NEE must be an integer times the grid size ND.	(84°)
NITR	The number of tidal constituent periods over which the integration is to proceed.	(1.)
N1	Grid point number (in compacted form) to be sampled for a time series analysis.	(1.)
N2	Grid point number (in compacted form) to be sampled for a time series analysis.	(2.)
N3	Grid point number (in compacted form) to be sampled for a time series analysis.	(3.)
ITYPE	Species of tidal component being integrated. 2 - diurnal 3 - semi-diurnal	(3.)
H2	Love number which represents the coefficient of uplift response of the solid earth to a non-loading potential.	(0.)

Table X
MODULE II NAMELIST VARIABLES

Variable Name	Function	Default Value
BR	Radius of the earth in meters (should be the same value used to generate the tidal solution from Module I.	(6371×10^3)
NOO	Lower latitude limit in degrees for global integration. (Must be the same value used to generate the tidal solution from Module I.	(-78°)
NEE	Upper latitude limit in degrees for global integration. (Must be the same value used to generate the tidal solution from Module I.	(84°)
GFCNG	Greens Function Flag 0. - Use default Greens function (See Table III) 1. - Use input values of ϕ' and U' functions to calculate Greens function.	$(0.)$
GFHP	U' Input Flag (Valid ONLY IF GFING = 1.) 0. - Set U' to zero in the Greens Function 1. - Input U' as a function of angle $(0^\circ - 180^\circ)$ in increments of 1° [FORMAT 8F10.3] in units $U'(\theta) * A * \theta * 10^{12}$.	$(1.)$
GFKP	ϕ' Input Flag (Valid ONLY IF GFCNG = 1.) 0. - Set ϕ' to zero in the Greens Function 1. - Input ϕ' as a function of angle $(0^\circ - 180^\circ)$ in increments of 1° [FORMAT 8F10.3] in units $\phi'(\theta) * A * \theta * 10^{12}$.	$(1.)$
GFSG	Self-Gravitation Term Flag 0. - Set self-gravitation term to zero in the Greens Function. 1. - Include self-gravitation term in the Greens Function.	$(1.)$

5.2 Program Output

The data output from the integration algorithm over the ocean grid network is voluminous and difficult to analyze in raw form. This necessitates plotted displays for visual analysis of the solution. In particular, the principal outputs are the cotidal and corange solution contours and the tidal time series plots for selected geographic points which are output to a plot tape for interface with an external plotting device. In addition, the integrator time t and the variables u , v , ξ and $h+\xi$ are output to tape in their compacted ocean arrays at the end of each integration period for program restart purposes. Additionally, the tidal time series is output on tape at the termination of the integration.

Printed plots are also produced for every plot output to the external plotting device. In addition, the program prints the total world function and the world grid of the ocean depth values for user inspection prior to calling the integration algorithm. At the end of each integration period the variables u , v and ξ are printed in their compacted ocean arrays, and then are printed in a full world grid array display.

7.0 ACKNOWLEDGEMENT

This work was performed under NASA Contract NAS 5-20045. The author wishes to acknowledge the support given by NASA/Goddard Space Flight Center in the investigation of ocean tide models, and in particular, it is with pleasure that the author acknowledges the interesting discussions and exchange of ideas with Dr. Peter Musen, who served as the contract technical officer in this effort.

7.0 REFERENCES

1. Admiralty Tide Tables, Hydrographic Department, Ministry of Defense, London.
2. Bogdanov, K. T. and Magarik, V., "Numerical Solutions to the Problem of Distribution of Semidiurnal Tides M_2 and S_2 in the World Ocean," Dokl. Akad. Nauk SSSR, 172. pp. 1315-1317, 1967.
3. Bogdanov, K. T. and Magarik, V., "A Numerical Solution of the Problem of Tidal Wave Propagation in the World Oceans, " Acad. Sci USSR and Oceanic Phys, Vol. 5, No. 12, pp. 1309-1319, 1969.
4. Cartwright, D. E. and Taylor, R. J., "New Computations of the Tide-Generating Potential," Geophys. J. Roy. Astr. Society, 23, pp. 45-74, 1971.
5. Defant, A., Physical Oceanography, Pergamon Press, New York, 1961.
6. Dietrich, G., "Die Gezeiten des Weltmeeres als geograph. Erscheinung." Z. d. ges. Erdkunde, pg. 69, Berlin, 1944.
7. Doodson, A. T., "The Harmonic Development of the Tide Generating Potential," Proc. Royal Society of London, Ser. A, 100, pp. 305-329, 1921.
8. Estes, R., "Computation of M_2 and K_1 Ocean Tidal Perturbations in Satellite Elements," Contract NAS 5-20045, BTS-TR-74-13, August 1974.
9. Estes, R., "A Computer Software System for the Generation of Global Numerical Solutions of Diurnal and Semidiurnal Ocean Tides," Contract NAS5-20045, BTS-TR-75-27, December 1975.
10. Farrell, W. E., "Deformation of the Earth by Surface Loads," Reviews of Geophysics and Space Physics, Vol. 10, No. 3, pp. 761, August 1972.
11. Felsentreger, T., Marsh, J. and Agreen, R., "Analyses of the Solid Earth and Ocean Tidal Perturbations on the Orbits of the GEOS-I and GEOS-II Satellites," X-921-75-194, (GSFC), July 1975.
12. Hansen, W., Symp. Math. Hydrodynam, Meth. Phys. Oceanog., Hamburg, pp. 25-34 (1961).
13. Hatch, W., "Statistical Characteristics of Skylab S-193 Altimeter Measurement Process," Contract NAS 6-2631, BTS-TR-73-23, June 1975.
14. Hendershott, M., "Ocean Tides," EOS, Vol. 54, No. 2, February 1973.
15. Hendershott, M. C., "The Effects of Solid Earth Deformation on Global Ocean Tides," Geophysical Journal Royal Astronomical Society, 29, pp. 389-403, 1972.
16. Hendershott, M. and Munk, W., "TIDES," Annual Review of Fluid Dynamics, Vol. 2, pp. 205-224, 1970.

17. Lambeck, K. and Casenave, A., "Fluid Tidal Effects on Satellite Orbit and Other Temporal Variations in the Geopotential, " G.R.G.S., No. 7, January 1973.
18. Lambeck, K., Cazenave, A. and Balmino, G., "Solid Earth and Ocean Tides Estimated from Satellite Orbit Analyses," Rev. Geophys. and Space Phys., Vol. 12, No. 3, pp. 420-434, 1974.
19. Longman, I. M., "A Green's Function for Determining the Deformation of the Earth Under Surface Mass Loads," J. G. R., 68, pp. 485, 1963.
20. Musen, P., "A Semi-Analytical Method of Computation of Oceanic Tidal Perturbations in the Motion of Artificial Satellites, " NASA-X-590-73-190 (GSFC), 1973.
21. Pekeris, C. L. and Accad, Y., "Solution of Laplace Equations for the M_2 Tide in the World Oceans," Phil. Trans. A265, pp. 413-436, 1969.
22. Platzman, G. W., "Ocean Tides and Related Waves," Lect. Appl. Math., American Mathematical Society, Providence, R. I., 1971.
23. Shanks, D., "Non-Linear Transformations of Divergent and Slowly Convergent Sequences," J. of Mathematics and Physics, Vol. 34, pp. 1-42, 1955.
24. Wunsch, C., "The Long Period Tides," Rev. Geophys., 5(4), pp. 447-475, 1967.
25. Zahel, W., "Die Reproduktion Gezeitenbedingter Bewegungsvorgänge in Weltozean Mittels des Hydrodynamisch - Numerischen Verfahrens," Mitt. Inst. Meereskunde der Univ. Hamburg, 17, 1970.
26. Zahel, W., "The Diurnal K_1 Tide in the World Ocean - A Numerical Investigation," Pure and Applied Geophysics, pp. 1819-1826, 1974.